Replica symmetry breaking in a quantum-optical vector spin glass

Ronen M. Kroeze,[1,2] Brendan P. Marsh,[2,3] David Atri Schuller,[2,3] Henry S. Hunt,[1,2]
Sarang Gopalakrishnan,[4] Jonathan Keeling,[5] and Benjamin L. Lev[1,2,3]

[1]*Department of Physics, Stanford University, Stanford CA 94305, USA*
[2]*E. L. Ginzton Laboratory, Stanford University, Stanford, CA 94305, USA*
[3]*Department of Applied Physics, Stanford University, Stanford CA 94305, USA*
[4]*Department of Electrical and Computer Engineering,*
Princeton University, Princeton NJ 08544, USA
[5]*SUPA, School of Physics and Astronomy, University of St. Andrews, St. Andrews KY16 9SS, United Kingdom*
(Dated: November 8, 2023)

Spin glasses are canonical examples of complex matter [1]. Although much about their structure remains uncertain, they inform the description of a wide array of complex phenomena, ranging from magnetic ordering in metals with impurities [2] to aspects of evolution, protein folding, climate models [1, 3], combinatorial optimization [4, 5], and artificial intelligence. Indeed, spin glass theory forms a mathematical basis for neuromorphic computing and brain modeling [6–10]. Advancing experimental insight into their structure requires repeatable control over microscopic degrees of freedom. Here, we achieve this at the atomic level using a quantum-optical system comprised of ultracold gases of atoms coupled via photons resonating within a confocal cavity. This active quantum gas microscope [11] realizes an unusual type of transverse-field vector spin glass with all-to-all connectivity. Spin configurations are observed in cavity emission and reveal the emergence of replica symmetry breaking and nascent ultrametric structure as signatures of spin-glass order [3]. The driven-dissipative nature of the system manifests as a nonthermal Parisi distribution, in qualitative correspondence with Monte Carlo simulations. The controllability provided by this new spin-glass system, potentially down to the quantum-spin-level [12], enables the study of spin-glass physics in novel regimes with application to quantum neural network computing [13].

The Sherrington-Kirkpatrick (SK) spin-glass model describes an all-to-all spin network with couplings of random sign [3, 14]. A rugged free energy landscape arises due to quenched disorder and geometric frustration. Ergodicity is broken: When cooled, exact system copies may relax into distinct thermodynamic regions of the high-dimensional spin-configuration space. These copies, called replicas, can be nonidentical (not merely under a global spin flip). Surprisingly, the overlaps among replica configurations exhibit an ultrametric, tree-like structure that emerges below the critical temperature T_c separating the SK spin glass from the paramagnet [15]. This is replica symmetry breaking (RSB), the phenomenon Parisi proposed in the 1970's and 80's as the first solution to a spin glass model; the theory's broad application to complex systems earned Parisi the 2021 Nobel Prize [16].

That replicas of a system are different, yet delicately correlated, is a bizarre consequence of the nonlocal, infinite-dimensional nature of the SK model. Determining whether some form of RSB exists for 3D materials with short-range coupling remains a grand challenge in statistical physics; other spin-glass theories are hard to distinguish from RSB scenarios using numerical simulation [1, 18]. A resolution might require experimental input, though lack of microscopic control hampers experiment-theory comparison.

Spin frustration and disorder have been separately realized in controllable systems using trapped ions [19, 20] and cavity-coupled atoms [21]. We simultaneously achieve both using multimode, confocal cavity QED, as suggested in [12, 13, 22–24] and discussed further
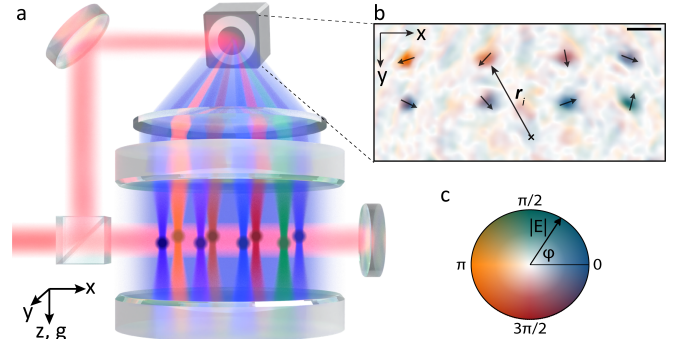

FIG. 1. Experimental system and spin detection. (a) Sketch of the confocal cavity QED apparatus. Atomic gases (eight colored balls) at vertex positions $\mathbf{r}_i$ of the network are pumped with a transverse field (red) and scatter light into local (multicolored) and nonlocal (light blue) components of the cavity field. Neither the mirror-image field components at $-\mathbf{r}_i$ nor the lasers trapping the atomic gases are shown. A portion of the pump mixes with cavity emission and illuminates a camera for holographic imaging; Ref. [17] discusses the analysis required to account for optical aberrations and spin-angle inhomogeneities. (b) Example of a reconstructed hologram of cavity emission for a coupled network of eight atomic gases. The eight bright spots are the local fields coupled to each gas. The arrows here and below indicate the spin vector direction θ derived from the electric field phase φ. The scale bar length here and below is w_0. (c) Color map indicating the electric field amplitude |E| and phase.

in [25–27]. Moreover, while RSB in nonlinear optical

devices has been reported for non-SK systems [28–31] (and incipient glassiness in networks of superconducting circuits [32, 33]), we observe RSB with minute programmable control over the quenched disorder. Microscopic spin readout from our quantum-optical system allows for direct experimental comparison to SK predictions. Its driven-dissipative nature manifests in nonthermal order parameter distributions. While this work addresses long-range spin-glass physics, it opens the door to experimental explorations of the order in short-range 3D spin glasses as well as those exhibiting quantum spin correlations and dynamics [12].

Figure 1a sketches the apparatus and Ref. [17] discusses the confocal cavity QED system in detail. Briefly, a pair of mirrors separated a distance equal to their radius of curvature confine many electromagnetic modes at nearly the same frequency. An array of optical dipole traps place $n = 8$ ultracold gases of ^{87}Rb atoms at different locations $\mathbf{r}_i$ within the cavity midplane $z = 0$. These form the n vertices of the spin network. Each vertex contains $N = 2.3(1) \times 10^5$ atoms within a radius $\sigma_A \approx 4\ \mu$m centered at $\mathbf{r}_i$. They are evaporatively cooled to slightly below the Bose-condensation temperature [17]—matterwave coherence is unimportant to this work.

A standing-wave transverse pump at $\lambda = 780$ nm and oriented along $\hat{x}$ scatters photons off the atoms in each vertex and into a superposition of cavity modes that is peaked at that location [11, 24]. When we linearly increase the pump's power $\propto \Omega^2$ through the superradiant threshold of a Hepp-Lieb-Dicke transition [34], the atoms in each vertex i spontaneously break translation symmetry by spatially ordering into a density wave along $\hat{z}$. The atoms choose a spatial phase θ_i that maximizes the local field amplitude at the vertex's position. However, the field of the confocal cavity is not perfectly localized and has a weaker, long-distance tail that is quasirandom in space [24, 35, 36]. When there are two vertices in the cavity, the nonlocal, long-range part of the field due to vertex 1 explicitly breaks the translational symmetry for vertex 2 and vice-versa. This leads to an interaction J_{12} between the symmetry-breaking phases of the two vertices [35, 36]; extending to many vertices directly follows.

Because the phases θ_i lie on a circle, we model each as an XY vector spin. The connection to a vector spin model is made by writing the photon-mediated interaction energy in terms of collective spin components $S_i^x = \cos\theta_i$ and $S_i^y = \sin\theta_i$:

$$E_{\text{int}} = -\sum_{i,j=1}^{n} \left[J_{ij}\left(S_i^x S_j^x - S_i^y S_j^y\right) + K_{ij}\left(S_i^x S_j^y + S_i^y S_j^x\right)\right],$$

(1)

where $J_{ij} \approx J_0 \cos R_{ij}$, $J_0 = N^2 g_0^2 \Omega^2/(8\Delta_A^2|\Delta_C|)$, and $R_{ij} = 2\mathbf{r}_i \cdot \mathbf{r}_j/w_0^2$. The $K_{ij} \approx (4\sigma_A^2/w_0^2)J_0 R_{ij}\sin R_{ij}$ term arises from the finite extent of each vertex in the imperfect confocal cavity. The total system energy is that of a transverse-field vector spin model with a transverse field strength proportional to E_{r}, the atomic recoil energy; see [17] for the full quantum Hamiltonian description.

Equation (1) applies in the far-detuned limit, where the pump is red-detuned by $\Delta_C = -2\pi\cdot 60$ MHz from the near-degenerate cavity resonances; both cavity and pump are $\Delta_A = -2\pi\cdot 97.3$ GHz from the atomic resonance. The waist w_0 of the cavity's fundamental mode is $35\ \mu$m, and g_0 is the single-atom coupling strength to this mode. The multimode single-atom cooperativity in the dispersive limit is $C_{\text{mm}} = 110$ [11]. Thus, this quantum-optical system acts as an active quantum gas microscope: The intracavity field mediates strong atomic interactions while the cavity's large effective numerical aperture allows us to holographically image the intracavity field at $z = 0$ with a resolution of 1.7 μm [11]. This is smaller than the width σ_A of each vertex. Figure 1b presents an example image taken at a pump power 25% above threshold, well within the spin-ordered phase.

We now discuss the phase portrait realized by Eq. (1). At small Ω, the system is in a normal (i.e., paramagnetic) phase that weakly scatters incoherent light into the cavity. Superradiant scattering ensues at large pumping strength, and the spins order either as a ferromagnet or spin glass depending on the values of J_{ij}. For K_{ij} sufficiently smaller than J_{ij}, as is the case here, Eq. (1) favors an x- (y-)ferromagnet when all $J_{ij} > 0$ (<0) or a spin glass when J_{ij} are disordered. By disorder, we mean J_{ij}'s that are both randomly signed and of random magnitude between $\pm J_0/N = \pm 2\pi\cdot 2.0(1)$ kHz. (This interaction timescale is several-times shorter than the few-hundred-μs interval between reaching threshold and beginning holographic imaging.)

Ferromagnets differ from paramagnets and spin glasses in their nonzero magnetization order parameter $m^\mu = \frac{1}{n}\sum_{i=1}^{n}\langle S_i^\mu\rangle$, where $\langle\cdot\rangle$ indicates time average and, for vector spins, we define $\mu \in \{x, y\}$. Distinguishing between the paramagnet and spin glass requires another order parameter, the spin overlap $q_{\alpha\beta}^{\mu\nu} = \frac{1}{n}\sum_{i=1}^{n}\langle S_i^{\alpha,\mu}\rangle\langle S_i^{\beta,\nu}\rangle$, where α and β are replica indices [3]. The overlap is always zero for a paramagnet but is nonzero for the ferromagnet and spin glass due to their frozen spin order. In the following we focus on two linear combinations of the overlap: $Q_{\alpha\beta} \equiv q_{\alpha\beta}^{xx} + q_{\alpha\beta}^{yy}$ and $R_{\alpha\beta} \equiv q_{\alpha\beta}^{yy} - q_{\alpha\beta}^{xx}$.

Before we present measurements of spin-overlap distributions, we discuss how these overlaps distinguish different phases. For an xy-vector ferromagnet, the spin-overlap distribution lies on the boundary of the square spanned by the allowed values of the overlap matrices, $|Q_{\alpha\beta}| \leq Q_{\alpha\alpha}$ and $|R_{\alpha\beta}| \leq |R_{\alpha\alpha}|$. Both $Q_{\alpha\alpha}$ and $|R_{\alpha\alpha}| = 1$ near $T = 0$ and in the measurements presented below. By contrast, a spin glass has nonzero overlaps in the interior of this square [37, 38]. This is the signature manifestation of RSB [3]: Even for identical initial conditions, thermal (or quantum) fluctuations during spin ordering drive replicas into distinct, energetically disconnected regions of the rugged free-energy landscape. This breaks ergodicity, yielding many non-spin-flip-symmetric

thermodynamic states that may be accessible to different replicas. Structure emerges from broken symmetry [39], and that which arises in the SK spin glass is the ultrametric structure of overlap distances $D_{\alpha\beta} = 1 - |Q_{\alpha\beta}|$ [40]. In other words, RSB implies that the $D_{\alpha\beta}$ satisfy the strong triangle inequality, $D_{\alpha\gamma} \leq \max\{D_{\alpha\beta}, D_{\beta\gamma}\}$, among any triplet of replicas.

Figures 2a,e present reconstructed images showing xFM and yFM states, resp. Repeating the experiment with identical positions allows us to compile a set of 900 replicas. We construct the magnetization and spin-overlap distributions shown in Figs. 2b,c,f,g. These exhibit the expected near-maximal magnetization and overlap 'goalposts' of ferromagnets at $q_{\alpha\beta}^{xx} = \pm 1$ ($q_{\alpha\beta}^{yy} = \pm 1$) for xFM (yFM). The slight tilt of the yFM magnetization, as well as the non-maximal $q_{\alpha\beta}^{yy}$'s, are caused by the K term [17]. Figures 2d,h show energy distributions of the xFM and yFM replicas, resp. While the minimum ferromagnetic energy is rarely found, the effective temperature is well within the ordered phase. (The paramagnet-to-ferromagnet T_c is found using parallel-tempering Monte Carlo [17].) The correspondence to an equilibrium distribution is remarkable despite the likely presence of technical noise and Landau-Zener transitions between nearby states at threshold. Cavity emission above threshold is known to couple the system to an effective thermal bath [13, 41], and the FM's near-thermal behavior might imply that a thermal-like, steady-state equilibrium has been reached.

We now create a spin glass by moving the vertices to realize a disordered J. Figures 3a–d show four distinct replicas of the same glassy J. These exemplify the multitude of configurations accessible within the glassy rugged landscape. The spin-overlap distributions in Figs. 3e–h are compiled from 100 experimental replicas each but are taken with different pump ramp rates. The rate used for panel (f) is the same as that used for the images in panels (a–d), as well as the ferromagnetic data in Fig. 2. This ramp rate is sufficiently slow to observe overlap peaks at $Q_{\alpha\beta} = \pm 1$, in addition to multiple $\alpha \neq \beta$ peaks in the distribution interior. This structure is consistent with the presence of RSB.

Increasing the ramp rate by a factor of two blurs these peaks while reducing the overlap goalposts, as seen in Fig. 3e. Presumably, more Landau-Zener transitions lead to a glass with higher-mean-energy $\langle E_{\text{int}} \rangle$ that explores more configurations in the rugged landscape. (We have not been able to ramp fast enough to image the paramagnet.) Conversely, slowing by a factor of two creates sharper, more sparse overlap peaks, as shown in Fig. 3g. Because we have a finite-sized system, RSB disappears when further slowing the ramp, producing distributions with lower $\langle E_{\text{int}} \rangle$. As shown in Fig 3h, the ground-state spin configuration dominates the distribution when $\langle E_{\text{int}} \rangle$ drops below the first excited state.

We now provide evidence for nascent ultrametric structure in the $Q_{\alpha\beta}$. Hierarchical clustering is performed to iteratively combine the replicas into groups that
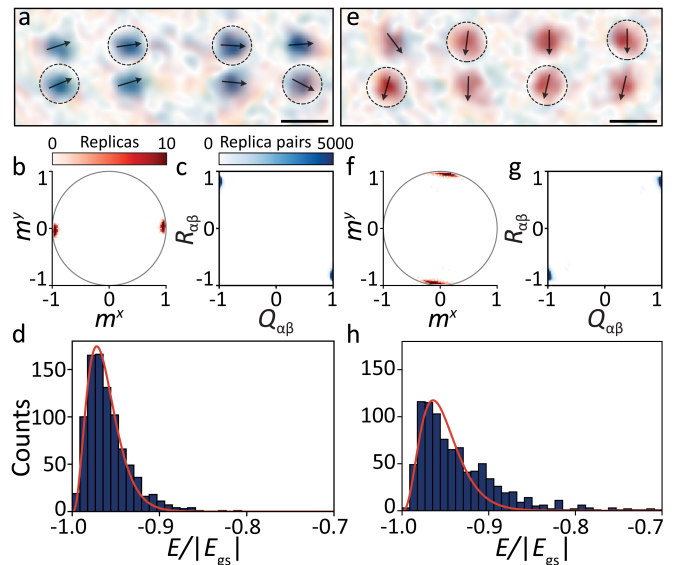

FIG. 2. Demonstration of two ferromagnetic states. (a–d) Data in support of an xFM-state arising from vertices positioned to realize an effective $J_{ij} > 0$ network. (a) Representative reconstructed image showing a cavity field with vertex phases of a spin configuration ordered along $\hat{x}$. A local π gauge rotation was applied to the vertices indicted by dashed circles [17]. (b) Magnetization distribution m^μ. (c) Distribution of overlap components $Q_{\alpha\beta}$ and $R_{\alpha\beta}$ between pairs of replicas. (d) Histogram of the energy of each xFM replica, normalized to the magnitude of their ground-state energies. Fitting with a Maxwell-Boltzmann distribution (red line) yields an effective temperature $T/T_c = 0.080(8)$. (e–h) Similar data for an effective $J_{ij} < 0$ network realizing a yFM state. (h) $T/T_c = 0.10(1)$.

minimize the average distance $1 - |Q_{\alpha\beta}|$ within those groups [42]. This allows the visualization of ultrametric relationships as block-diagonal structures in $|Q_{\alpha\beta}|$ [40]. This is shown in Figs. 3i–l; see Ref. [43] for the leaf sorting algorithm. For example, Fig. 3i shows at least six clusters. Off-diagonal rectangles of lighter shade provide evidence of multistep RSB structure; the three distinct shades indicate that at least three thermodynamics states contribute to the spin glass order [1, 44]. (The clustering hierarchy becomes trivial for the slow-ramp case in panel (l).)

Ultrametric structure may also be visualized as a family-tree-like dendrogram [1, 40]. These are shown above the $|Q_{\alpha\beta}|$ matrices. Replicas are the leaves at the lowest generation level. The overlap between two replicas is approximately the value of the distance of the topmost branch connecting them. Limbs are colored to denote near-kin families, which are the emergent clusters of $|Q_{\alpha\beta}|$. A quantitative analysis based on the strong triangle inequality [45] is presented in [17].

Figures 4b–d show overlap distributions for three additional realizations of disordered J-matrices. They differ from both each other and the overlap in Fig. 3f (reproduced in panel 4a), demonstrating the strong dependence
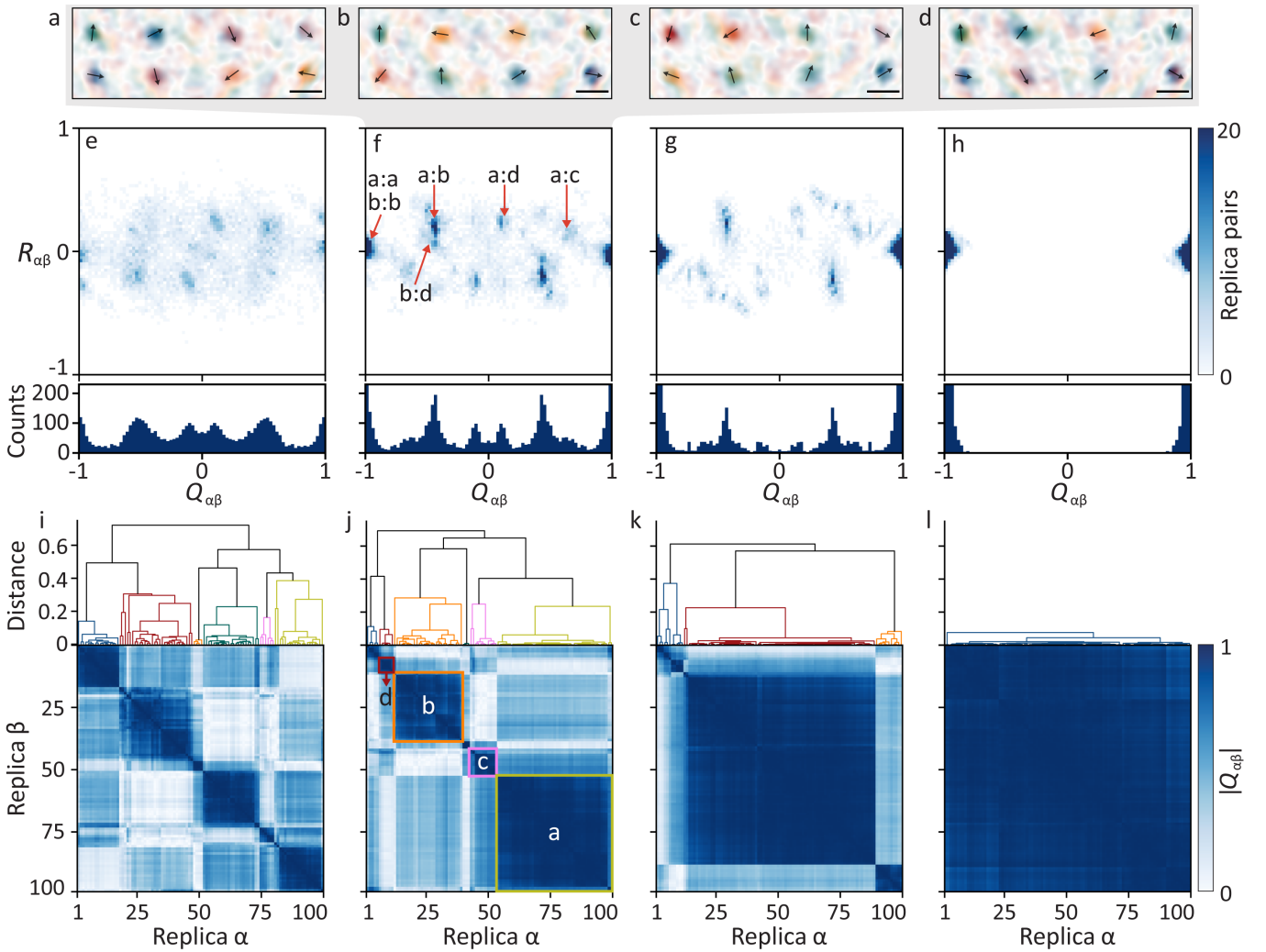
FIG. 3. Spin-overlap distributions of the vector spin glass versus ramp rate. (a–d) Reconstructed images of the four most commonly found spin configurations for the same representative disordered J. These spin states are found in 45%, 26%, 9%, and 5% of the 100-total experimental replicas, resp. (e–h) Overlap distributions versus ramp rate for the same disordered J. The rate of increase of the pump lattice depth is, in E_r/ms: (e), 1100; (f), 45; (g), 23; and (h), 11. The mean energies $\langle E_{\text{int}} \rangle$ of these states, normalized by the ground-state energy $|E_{\text{gs}}|$, are: (e), -0.75(1); (f), -0.84(1); (g), -0.88(1); and (h), -0.926(4). Panel (f) also indicates the particular replica pairs from panels (a–d) contributing to each major peak. The peaks are denoted $\alpha:\beta$ using the panel tags a, b, c, and d as replica labels. Shown below are the 1D marginal distributions; i.e., histograms of the number of replica pairs at each value of $Q_{\alpha\beta}$. (i-l) Hierarchically clustered $|Q_{\alpha\beta}|$ matrices with family-tree-like dendrograms are shown for each ramp rate. The states in panels (a–d) are contained in the four distinct clusters outlined with squares in panel (j). The squares are color-coded to match the associated branch of the family-tree-like dendrogram drawn above. The distance of each branch is calculated based on the average of overlaps within the limb below it. Color-coding is used for families below a distance of 0.4, which corresponds to clusters with spin configurations separated by approximately two spin flips.

of spin overlaps on disorder realization. This is expected of a glass, where the energy gaps and rugged-landscape topography can sensitively depend on disorder details.

Attempts to accurately simulate these overlaps with parallel-tempering Monte Carlo [46, 47] based on Eq. (1) are hampered by the inherently nonequilibrium nature of the experiment. That is, once glassy, this driven-dissipative system may not necessarily yield spin configurations corresponding to a thermal equilibrium. Indeed, we find that there is no simulated temperature at which

all features are reproduced correctly [17]. At high temperature, all peaks are reproduced, but they are blurred due to thermal fluctuations. While the peaks are sharper at low temperature, some overlap peaks are missing since they arise from higher-energy configurations. Instead, we perform an ad hoc simulation that mimics some nonequilibrium effects by halting a rapid-annealing simulation before it reaches equilibrium [17]. The simulation uses the J and K-matrices derived from direct observations for each disorder realization [17]. The resulting numer-
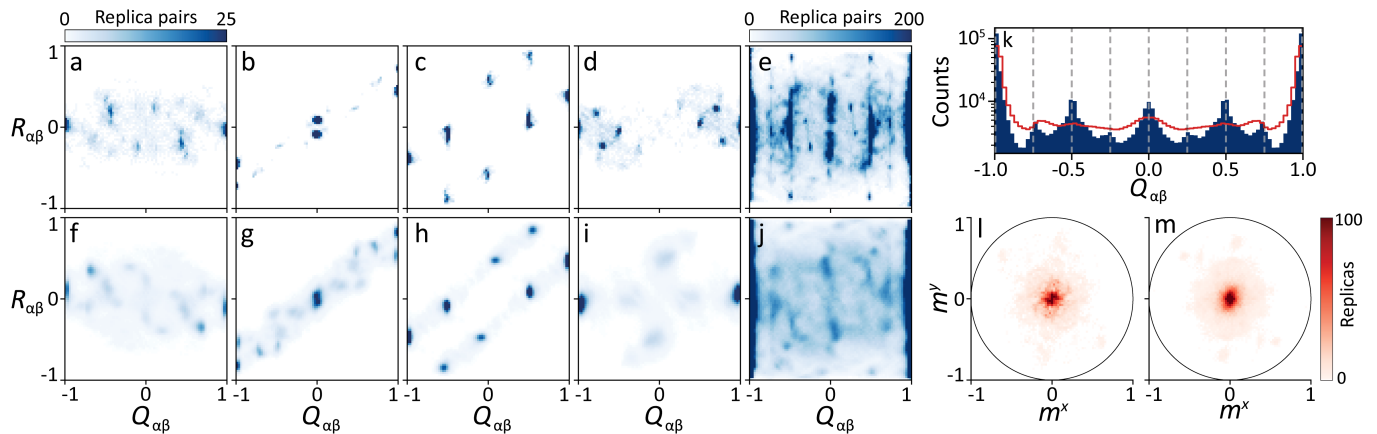
FIG. 4. Comparison of experimental and simulated spin overlaps and Parisi order parameters. (a-d) Each of these experimental overlap distributions is realized by moving the vertices to different sets of positions that realize four different disorder realizations J. Each of these overlaps are derived from 100 experimental replicas and share the same color scale. (e) The experimental Parisi order parameter distribution formed by averaging 123 overlap distributions, each with a different disordered J-matrix. (f–i) Numerical simulations using as input the experimentally measured Js in panels (a-d). (j) Numerical simulation of the Parisi order parameter distribution using J-matrices calculated from observed positions. (k) 1D marginal histogram of the Parisi order parameter distribution in panel (e). Dashed lines indicate allowed overlap values for a binarized (Ising) 8-spin system. The red trace is the 1D marginal histogram from panel (j). (l) Experimental and (m) numerical magnetization distributions averaged over the same experimental ensemble as above.

ical overlap distributions are shown in Figs. 4f–i. The results in panels (f–h) are in qualitative agreement with the experimental ensemble, but some, like that in panel (i), are far off.

Specific disorder details cease to play a role in the large system-size limit of non-glassy systems. By contrast, the values of $q_{\alpha\beta}^{\mu\nu}$ are different for different disorder realizations of J, implying a lack of self-averaging because multiple thermodynamic states contribute. A thermodynamic quantity that is independent of microscopic disorder details appears if we take the disorder average $\langle q_{\mu\nu}^{\alpha\beta}\rangle_J$ over all J realizations. This is the Parisi order parameter [48], which exhibits a smooth distribution of $Q_{\alpha\beta}$ between the $\pm Q_{\alpha\alpha}$ goalposts and whose shape is determined by temperature via the Gibbs measure [1].

To measure the Parisi order parameter, we average the experimental overlap distributions in Fig. 4a–d, plus 119 others (each compiled from 100 experimental replicas). The result is shown in Fig. 4e; see [17] for assessment of ensemble randomness and convergence. The 1D marginal distribution in Fig. 4k exhibits continuous support between the overlap goalposts; this signature of RSB is also found in the Parisi distribution of an SK Ising spin glass [1]. However, we observe several peaks between the goalposts rather than a smooth distribution. Overlaid on the plot are $n + 1 = 9$ equally spaced vertical dashed lines set at the allowed overlap-value locations that would be found in an Ising network of $n = 8$ vertices. That the peaks in the data match these positions suggests that the vector spins are weakly binarized along the Q quadrature.

A Monte Carlo simulation using a rapid-annealing schedule is shown in Fig. 4j and reproduces some of this striped behavior, as is clear from the marginal shown in

red in Fig. 4k. (As above, the simulation uses the experimentally characterized J and K-matrices [17].) Simulation discrepancies might also arise from an unidentified easy-axis energy term or from nonlinearities arising during the imaging sequence [17]. Alternatively, the stripe effect could be intrinsic to the nonequilibrium system. A parallel-tempering simulation also failed to faithfully reproduce the data [17]. As with the overlap distributions, it seems that neither an equilibrium (parallel tempering) nor a nonequilibrium (rapid simulated annealing) simulation reproduces all details of the experimental Parisi order parameter distribution.

A spin glass should also have zero average magnetization. The experimental disorder-averaged vector magnetization is shown in Figs. 4l, and it is centered around $\mathbf{m} = 0$ as expected. In contrast to overlaps, simulations similar to those performed above do capture the magnetization distribution width; see Fig. 4m.

Future work will attempt to improve the correspondence with simulation by developing more sophisticated nonequilibrium numerical techniques and by experimentally exploring longer-term spin evolution. Improvements to atom trapping and cavity-emission imaging will enable larger network sizes. Measurements of dynamical susceptibility may reveal aging effects in this novel vector spin glass. Last, we note it is possible to realize short-range, RKKY-like interactions [49], and we have already created small, frustrated Ising-spin networks in this confocal cavity QED system [50].

[1] D. L. Stein and C. M. Newman, *Spin Glasses and Complexity*, Primers in Complex Systems (Princeton University Press, 2013).

[2] K. H. Fischer and J. A. Hertz, *Spin Glasses* (Cambridge University Press, Cambridge, 1991).

[3] P. Charbonneau, E. Marinari, M. Mézard, G. Parisi, F. Ricci-Tersenghi, G. Sicuro, and F. Zamponi, *Spin Glass Theory and Far Beyond* (World Scientific, 2023).

[4] F. Barahona, "On the computational complexity of Ising spin glass models," J. Phys. A: Math. Gen. **15**, 3241 (1982).

[5] A. Lucas, "Ising formulations of many NP problems," Front. Physics **2**, 1 (2014).

[6] J. J. Hopfield, "Neural networks and physical systems with emergent collective computational abilities." Proc. Natl. Acad. Sci. U.S.A. **79**, 2554 (1982).

[7] J. Hopfield and D. Tank, "Computing with neural circuits: a model," Science **233**, 625 (1986).

[8] D. J. Amit, *Modeling Brain Function* (Cambridge University Press, 1989).

[9] J. Hertz, A. Krogh, and R. Palmer, *Introduction To The Theory Of Neural Computation*, Addison-Wesley Computation and Neural Systems Series (Avalon Publishing, 1991).

[10] Y. Bahri, J. Kadmon, J. Pennington, S. S. Schoenholz, J. Sohl-Dickstein, and S. Ganguli, "Statistical Mechanics of Deep Learning," Annu. Rev. Condens. Matter Phys. **11**, 501 (2020).

[11] R. M. Kroeze, B. P. Marsh, K.-Y. Lin, J. Keeling, and B. L. Lev, "High Cooperativity Using a Confocal-Cavity–QED Microscope," PRX Quantum **4**, 020326 (2023).

[12] B. P. Marsh, R. M. Kroeze, S. Ganguli, S. Gopalakrishnan, J. Keeling, and B. L. Lev, "Entanglement and replica symmetry breaking in a driven-dissipative quantum spin glass," (2023), arXiv:2307.10176.

[13] B. P. Marsh, Y. Guo, R. M. Kroeze, S. Gopalakrishnan, S. Ganguli, J. Keeling, and B. L. Lev, "Enhancing Associative Memory Recall and Storage Capacity Using Confocal Cavity QED," Phys. Rev. X **11**, 021048 (2021).

[14] D. Sherrington and S. Kirkpatrick, "Solvable Model of a Spin-Glass," Phys. Rev. Lett. **35**, 1792 (1975).

[15] M. Mezard, G. Parisi, and M. Virasoro, *Spin Glass Theory And Beyond: An Introduction To The Replica Method And Its Applications*, World Scientific Lecture Notes In Physics (World Scientific Publishing Company, 1987).

[16] G. Parisi, "Nobel Lecture: Multiple equilibria," Rev. Mod. Phys. **95**, 030501 (2023).

[17] See Supplementary Information for experimental details and numerical simulations.

[18] P. Contucci and C. Giardinà, *Perspectives on Spin Glasses*, Perspectives on Spin Glasses (Cambridge University Press, 2013).

[19] K. Kim, M.-S. Chang, S. Korenblit, R. Islam, E. E. Edwards, J. K. Freericks, G.-D. Lin, L.-M. Duan, and C. Monroe, "Quantum simulation of frustrated Ising spins with trapped ions," Nature **465**, 590 (2010).

[20] R. Islam, C. Senko, W. C. Campbell, S. Korenblit, J. Smith, A. Lee, E. E. Edwards, C.-C. J. Wang, J. K. Freericks, and C. Monroe, "Emergence and Frustration of Magnetism with Variable-Range Interactions in a Quantum Simulator," Science **340**, 583 (2013).

[21] N. Sauerwein, F. Orsi, P. Uhrich, S. Bandyopadhyay, F. Mattiotti, T. Cantat-Moltrecht, G. Pupillo, P. Hauke, and J.-P. Brantut, "Engineering random spin models with atoms in a high-finesse cavity," Nat. Phys. **19**, 1128 (2023).

[22] S. Gopalakrishnan, B. L. Lev, and P. M. Goldbart, "Frustration and Glassiness in Spin Models with Cavity-Mediated Interactions," Phys. Rev. Lett. **107**, 277201 (2011).

[23] S. Gopalakrishnan, B. L. Lev, and P. M. Goldbart, "Exploring models of associative memory via cavity quantum electrodynamics," Philos. Mag. **92**, 353 (2012).

[24] V. D. Vaidya, Y. Guo, R. M. Kroeze, K. E. Ballantine, A. J. Kollár, J. Keeling, and B. L. Lev, "Tunable-Range, Photon-Mediated Atomic Interactions in Multimode Cavity QED," Phys. Rev. X **8**, 011002 (2018).

[25] P. Strack and S. Sachdev, "Dicke Quantum Spin Glass of Atoms and Photons," Phys. Rev. Lett. **107**, 277202 (2011).

[26] P. Rotondo, E. Tesio, and S. Caracciolo, "Replica symmetry breaking in cold atoms and spin glasses," Phys. Rev. B **91**, 014415 (2015).

[27] V. Erba, M. Pastore, and P. Rotondo, "Self-Induced Glassy Phase in Multimodal Cavity Quantum Electrodynamics," Phys. Rev. Lett. **126**, 183601 (2021).

[28] N. Ghofraniha, I. Viola, F. Di Maria, G. Barbarella, G. Gigli, L. Leuzzi, and C. Conti, "Experimental evidence of replica symmetry breaking in random lasers," Nat. Commun. **6**, 6058 (2015).

[29] A. S. L. Gomes, E. P. Raposo, A. L. Moura, S. I. Fewo, P. I. R. Pincheira, V. Jerez, L. J. Q. Maia, and C. B. de Araújo, "Observation of Lévy distribution and replica symmetry breaking in random lasers from a single set of measurements," Sci. Rep. **6**, 27987 (2016).

[30] D. Pierangeli, A. Tavani, F. Di Mei, A. J. Agranat, C. Conti, and E. DelRe, "Observation of replica symmetry breaking in disordered nonlinear wave propagation," Nat. Commun. **8**, 1501 (2017).

[31] J. Niedda, "Realistic Model for Random Lasers from Spin-Glass Theory," (2023), arXiv:2306.08972.

[32] R. Harris *et al.*, "Phase transitions in a programmable quantum spin glass simulator," Science **361**, 162 (2018).

[33] A. D. King *et al.*, "Quantum critical dynamics in a 5,000-qubit programmable spin glass," Nature **617**, 61 (2023).

[34] F. Mivehvar, F. Piazza, T. Donner, and H. Ritsch, "Cavity QED with quantum gases: new paradigms in many-body physics," Adv. Phys. **70**, 1 (2021).

[35] Y. Guo, R. M. Kroeze, V. D. Vaidya, J. Keeling, and B. L. Lev, "Sign-Changing Photon-Mediated Atom Interactions in Multimode Cavity Quantum Electrodynamics," Phys. Rev. Lett. **122**, 193601 (2019).

[36] Y. Guo, V. D. Vaidya, R. M. Kroeze, R. A. Lunney, B. L. Lev, and J. Keeling, "Emergent and broken symmetries of atomic self-organization arising from Gouy phase shifts in multimode cavity QED," Phys. Rev. A **99**, 053818 (2019).

[37] J. M. Kosterlitz, D. J. Thouless, and R. C. Jones, "Spherical Model of a Spin-Glass," Phys. Rev. Lett. **36**, 1217 (1976).

[38] S. Kirkpatrick and D. Sherrington, "Infinite-ranged models of spin-glasses," Phys. Rev. B **17**, 4384 (1978).

[39] P. M. Chaikin and T. C. Lubensky, *Principles of Condensed Matter Physics* (Cambridge University Press, 1995).

[40] R. Rammal, G. Toulouse, and M. A. Virasoro, "Ultrametricity for physicists," Rev. Mod. Phys. **58**, 765 (1986).

[41] E. G. Dalla Torre, S. Diehl, M. D. Lukin, S. Sachdev, and P. Strack, "Keldysh approach for nonequilibrium phase transitions in quantum optics: Beyond the Dicke model in optical cavities," Phys. Rev. A **87**, 023831 (2013).

[42] F. Murtagh and P. Contreras, "Algorithms for hierarchical clustering: an overview," WIREs Data Mining Knowl Discov **2**, 86 (2011).

[43] Z. Bar-Joseph, D. K. Gifford, and T. S. Jaakkola, "Fast optimal leaf ordering for hierarchical clustering," Bioinformatics **17**, S22 (2001).

[44] G. Parisi, "A sequence of approximated solutions to the S-K model for spin glasses," J. Phys. A: Math. Gen. **13**, L115 (1980).

[45] H. G. Katzgraber and A. K. Hartmann, "Ultrametricity and Clustering of States in Spin Glasses: A One-Dimensional View," Phys. Rev. Lett. **102**, 037207 (2009).

[46] R. H. Swendsen and J.-S. Wang, "Replica Monte Carlo Simulation of Spin-Glasses," Phys. Rev. Lett. **57**, 2607 (1986).

[47] K. Hukushima and K. Nemoto, "Exchange Monte Carlo Method and Application to Spin Glass Simulations," J. Phys. Soc. Jpn. **65**, 1604 (1996).

[48] D. Elderfield and D. Sherrington, "The Parisi overlap function for vector spin glasses," J. Phys. C: Solid State Phys. **17**, 5595 (1984).

[49] M. A. Ruderman and C. Kittel, "Indirect Exchange Coupling of Nuclear Magnetic Moments by Conduction Electrons," Phys. Rev. **96**, 99 (1954).

[50] R. M. Kroeze, "Many-body spin physics with quantum gases in a confocal cavity," Ph.D. Thesis, Department of Physics, Stanford University (2023).

[51] A. J. Kollár, A. T. Papageorge, K. Baumann, M. A. Armen, and B. L. Lev, "An adjustable-length cavity and Bose–Einstein condensate apparatus for multimode cavity QED," New J. Phys. **17**, 043012 (2015).

[52] F. Piazza, P. Strack, and W. Zwerger, "Bose–Einstein condensation versus Dicke–Hepp–Lieb transition in an optical cavity," Ann. Phys. **339**, 135 (2013).

[53] R. Landig, L. Hruby, N. Dogra, M. Landini, R. Mottl, T. Donner, and T. Esslinger, "Quantum phases from competing short- and long-range interactions in an optical lattice," Nature **532**, 476 (2016).

[54] R. M. Kroeze, Y. Guo, V. D. Vaidya, J. Keeling, and B. L. Lev, "Spinor Self-Ordering of a Quantum Gas in a Cavity," Phys. Rev. Lett. **121**, 163601 (2018).

[55] Y. Guo, R. M. Kroeze, B. P. Marsh, S. Gopalakrishnan, J. Keeling, and B. L. Lev, "An optical lattice with sound," Nature **599**, 211 (2021).

[56] K. Baumann, C. Guerlin, F. Brennecke, and T. Esslinger, "Dicke quantum phase transition with a superfluid gas in an optical cavity," Nature **464**, 1301 (2010).

[57] K. Baumann, R. Mottl, F. Brennecke, and T. Esslinger, "Exploring Symmetry Breaking at the Dicke Quantum Phase Transition," Phys. Rev. Lett. **107**, 140402 (2011).

[58] A. J. Kollár, A. T. Papageorge, V. D. Vaidya, Y. Guo, J. Keeling, and B. L. Lev, "Supermode-density-wave-polariton condensation with a Bose–Einstein condensate in a multimode cavity," Nat Commun **8**, 14386 (2017).

[59] R. M. Kroeze, Y. Guo, and B. L. Lev, "Dynamical Spin-Orbit Coupling of a Quantum Gas," Phys. Rev. Lett. **123**, 160404 (2019).

[60] I. Rozada, M. Aramon, J. Machta, and H. G. Katzgraber, "Effects of setting temperatures in the parallel tempering Monte Carlo algorithm," Phys. Rev. E **100**, 043311 (2019).

[61] K. Hukushima, "Domain-wall free energy of spin-glass models: Numerical method and boundary conditions," Phys. Rev. E **60**, 3606 (1999).

[62] N. Metropolis, A. W. Rosenbluth, M. N. Rosenbluth, A. H. Teller, and E. Teller, "Equation of state calculations by fast computing machines," J. Chem. Phys. **21**, 1087 (1953).

[63] W. K. Hastings, "Monte Carlo sampling methods using Markov chains and their applications," Biometrika **57**, 97 (1970).

[64] R. Cherrier, D. S. Dean, and A. Lefèvre, "Role of the interaction matrix in mean-field spin glass models," Phys. Rev. E **67**, 046112 (2003).

[65] H. G. Katzgraber, T. Jörg, F. Krząkała, and A. K. Hartmann, "Ultrametric probe of the spin-glass state in a field," Phys. Rev. B **86**, 184405 (2012).

SUPPLEMENTARY INFORMATION

CONTENTS

I. EXPERIMENTAL METHODS

A. BEC preparation

Atom cooling and trapping follows Refs. [35, 51] with additional steps taken to produce eight atomic clouds that serve as the spin network vertices. We employ time-multiplexed RF signals produced by voltage-controlled oscillators to drive acousto-optical modulators to dynamically shape the trap. Specifically, we begin by creating a cloud of $2.5(2) \times 10^6$ ^{87}Rb atoms at a temperature of 548(8) nK held in two dithered, crossed optical dipole traps. Subsequently, the dithered drive signals are adiabatically deformed into a step-ladder waveform with 2 and 4 steps, resp., resulting in the initial atomic cloud being split into a 2×4 grid of smaller, well-separated clouds. The amplitudes of the steps in the dither drive determine the vertex positions, while the duty cycle for each step controls the relative atomic population per vertex. The population in each resulting gas cloud is balanced to contain $\sim 2.3(1) \times 10^5$ atoms. Each has a temperature of 440(60) nK measured with time-of-flight imaging. This temperature is near the critical temperature for Bose-Einstein condensation (BEC), resulting in a BEC fraction of $\sim$11%. The relatively large thermal fraction causes a shift of the superradiant phase transition point [52], but does not further affect superradiance.
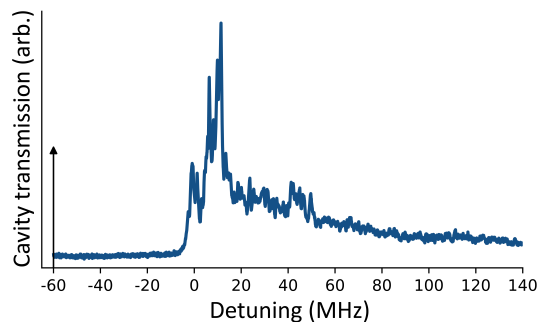
FIG. S5. Transmission spectroscopy of the confocal cavity used in this work. A spot of waist 32 μm aimed 80 μm radially from the cavity center is used to probe the cavity. The detuning of the transverse pump beam is indicated by the black arrow.

Some calibration experiments require isolating a single vertex, such as measuring trap frequencies and atomic shape, or for imaging the nonlocal field from a signal vertex. This is accomplished by first preparing the full network of eight vertices, then switching the RF drives to a single tone, instead of the time-multiplexed tones. This allows us to remove the trapping potential at all vertices but the site of interest. We then wait 400 ms to let the atoms in the other vertices fall under the force of gravity. The time-multiplexed RF drive is then reactivated to recover the precise original trap shape, but with only a single vertex populated.

Trap frequencies for each vertex are measured by first isolating the vertex of interest according to the above procedure. The atoms in the trap are then weakly excited to stimulate a sloshing mode. Momentum oscillations from time-of-flight imaging reveal the trap frequency. We observe vertex-to-vertex dependence of the trapping frequencies. This is caused by the way we create the traps by dithering the trapping beams between spatial locations. The beam spends more time in some locations than others to balance the atom populations across the vertices. However, this also changes the trap frequencies and depths: Typical frequencies are $[\omega_x, \omega_y, \omega_z] = 2\pi \times [296(10), 170(27), 170(8)]$ Hz, where the standard deviation is assessed over all eight sites and two different position configurations. Error below is also given as standard deviation.

The atomic shape at each vertex is described by a bimodal distribution. Thermal atoms contribute a Gaussian density component while the BEC fraction of the gas contributes a Thomas-Fermi component. To simplify calculations that involve the density profile, we approximate the bimodal distribution in the cavity transverse plane by an isotropic 2D Gaussian of 4-μm standard deviation along the trap directions. This width is determined by a least-squares fit to the full 2D bimodal distribution on the cavity midplane.

The $1/e$ lifetime of the atoms in an 8-vertex configuration is typically around 2 s. The transverse pump subjects the atoms to additional heating. This reduces the $1/e$ lifetime to 318(16) ms for a pump lattice depth of approximately $3.8E_\mathrm{r}$. Threshold is typically around $45E_\mathrm{r}$, and the superradiant emission decays with a $1/e$ timescale of 3.5(3) ms when holding the pump lattice depth at $1.25\times$ threshold.

B. Cavity and pump laser

We employ a near-confocal cavity [51] with a free spectral range (FSR) of $2\pi\cdot15.02980(8)$ GHz; its length and mirror radius' of curvature are both 1 cm. The finesse is approximately 5×10^4 and the single-mode cooperativity is $C = 2g_0^2/\kappa\Gamma \approx 5.2$. The single-atom, multimode light-matter coupling strength is $\sqrt{M}g_0$, where $g_0 = 2\pi\cdot1.47$ MHz and $M \approx 21$ is the multimode enhancement factor [11, 24]. The corresponding dispersive multimode single-atom cooperativity is $C_\mathrm{mm} = 2Mg_0^2/\kappa\Gamma = 110$ [11], where the cavity and atomic linewidths are $\kappa = 2\pi\cdot137$ kHz and $\Gamma = 2\pi\cdot6.1$ MHz.

The cavity length is stabilized using the Pound-Drever-Hall technique with a laser coupled to the cavity at 1560 nm [51]. The remaining light is amplified and frequency-doubled to provide the 780-nm transverse pump light. It is detuned from the $5^2S_{1/2}|2, -2\rangle$ to $5^2P_{3/2}|3, -3\rangle$ transition by $\Delta_A/2\pi = -98.3$ GHz. The pump is detuned from the cavity resonance by $\Delta_C/2\pi = -60$ MHz from the lowest frequency peak in the cavity transmission spectrum. An example cavity spectrum is shown in Fig. S5 for a longitudinal probe beam of waist $0.9w_0$ injected to the side of the cavity center.

The pump laser is retroreflected to produce a standing-wave optical lattice at the location of the atoms. The lattice depth is calibrated using Kapitza-Dirac diffraction of a BEC. During the experiment, and unless otherwise noted, the depth of the pump lattice linearly increases by $45E_\mathrm{r}$/ms for 1.5 ms. No Mott insulating phase arises at the Δ_C we employ [53]. After reaching $1.25\times$ the critical pump power, the holographic image is taken by rapidly
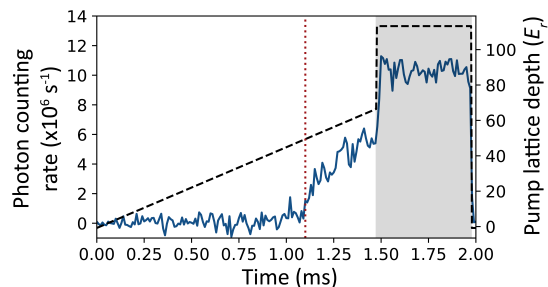
FIG. S6. Cavity emission intensity (left axis, blue solid line) detected by a single-photon counter versus time after subtracting background counts. The transverse pump power—in units of lattice depth (right axis, black dashed line)—is ramped linearly through the superradiant threshold. Threshold is demarcated by a sudden increase in cavity emission, indicated by the red dotted line. After ramping to 1.25× the threshold power, the state is read-out for 500 μs, as indicated by the gray shaded area. During the read-out process, the pump power is rapidly increased and the local oscillator and cavity emission expose the camera.

increasing the pump power to $113E_{\rm r}$ and holding there for 500 μs for readout of the spin state. The pump schedule is illustrated in Fig. S6 with an example of the measured cavity emission recorded on a single-photon counter. We have independently verified that this imaging process does not alter the spin-organized state: Any dynamics induced by the readout would result in reduction of fringe contrast for the evolving vertices. We do not observe such signal reduction, other than for all vertices simultaneously, which we attribute to reduced atom number in that particular experimental shot. Additionally, we measure the phase of the (spatially integrated) intracavity field using a temporal heterodyne measurement. These measurements show no observable phase difference between the moment just prior to the readout versus during the readout.

C. Holographic imaging

Detection of the spin state that emerges in the superradiant phase is achieved through holographic imaging of the emitted cavity field, as in our previous work [35, 36, 54, 55]. The emitted field is mixed with a local oscillator (LO) derived from the transverse pump and focused onto an electron-multiplied charge-coupled-device camera. The cavity field and LO strike the camera at slightly different angles to produce a phase-sensitive interference pattern, realizing a spatial heterodyne measurement. Sections I D and I F provide details about how the detected images are processed to extract the density wave (DW) phase for each vertex.

Optical components between the cavity and camera can cause phase aberrations in the detected holographic images. This aberration is characterized by positioning a single gas cloud of atoms at the cavity center and pumping the system above the superradiant threshold. The emitted cavity field for this particular configuration of atoms should have a completely flat phase front. Any additional phase must be due to aberrations. This becomes a phase mask that is subtracted from all holographic images.

D. Processing of holographic images and spin-state extraction

We now describe how we extract the spin configuration from a recorded holographic image. As we show in Sec. II B, the phase of the emitted cavity field is directly related to the spin configuration. Phase extraction is accomplished through a fit by least-squares regression to the full field-of-view of the emitted cavity field. We account for finite-size effects by allowing for DW phase gradients. A discussion of the origin of these gradients is presented in Sec. II A and Sec. II C.

As we derive in Sec. II B, the total field is a sum over the fields generated by each vertex,

$$\Phi^F(\mathbf{r}) = e^{i\phi} \sum_{i=1}^{n} A_i \left[e^{-i\theta_i} \Phi_{\rm local}(\mathbf{r}; \mathbf{r}_i) + e^{i\theta_i} \Phi_{\rm non}(\mathbf{r}; \mathbf{r}_i) \right], \tag{S2}$$

where the superscript F denotes that this is the forward-propagating field emitted from the cavity, ϕ is a global phase, A_i is the amplitude of the field and θ_i is the DW phase of vertex i, which is at position $\mathbf{r}_i$. While the emitted cavity field and LO have a stable phase within the time span of a single experimental shot, there is a slow drift of the
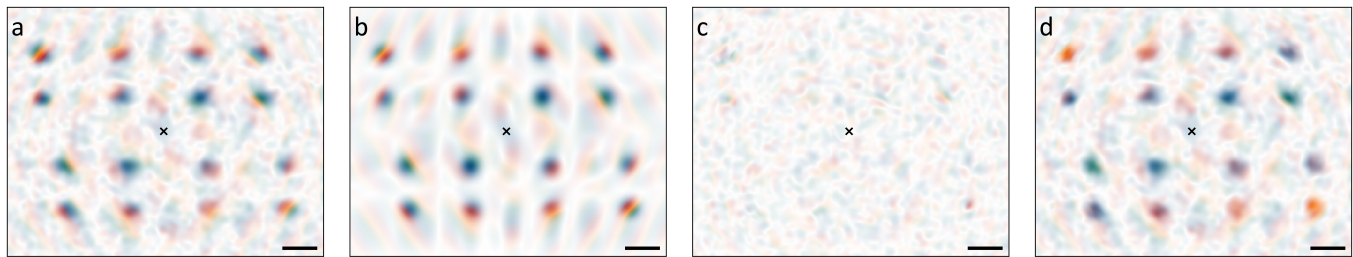
FIG. S7. Processing of holographic images. In all panels, the scale bar indicates $w_0 = 35\ \mu$m and cavity center is marked by a cross. (a) Raw holographic image of an emitted cavity field for the processed image presented in Fig. 1b of the main text. Each vertex scatters a localized spot, with a mirror-image spot on the opposite side of the cavity. The nonlocal component of the field produces a weaker background field present throughout the image. (b) Optimal fit obtained from the model given by Eq. (S2). (c) The residual between the measured and fitted images in panels (a) and (b), resp. The color scale is the same as in panel (a). (d) The resulting gradient-corrected holographic image. The upper half of this image is identical to that presented in Fig. 1b of the main text.

LO phase from shot-to-shot that results in a different global phase ϕ that must be fit for each image. The local and nonlocal field generated by vertex i are given by Eqs. (S36) and (S37). These further contain the Gaussian width of the vertex σ_A and the DW phase gradient $\mathbf{g}_i$. Equation (S2) is fit to the electric field obtained from holographic imaging to determine the global parameters ϕ and σ_A as well as the parameters for describing each vertex, $\{A_i, \theta_i, \mathbf{r}_i, \mathbf{g}_i\}$. The spin state corresponds to the DW phases θ_i. The extracted spin states are not random due to noise, as can be seen by the specific overlap structure in Figs. 3 and 4 of the main text.

An example hologram is shown in Fig. S7a with the corresponding best fit result in panel (b) and the residual in panel (c). To speed-up the fitting procedure, we downsample the observed electric field by averaging blocks of 3×3 pixels into single superpixels. Comparing the results from downsampled fits to full fits reveals no systematic bias, with an root-mean-square difference between these spin configurations of less than 0.002 radians per spin across a set of 30 images.

The images in Figs. 1–3 of the main text are corrected to remove the global phase ϕ as well as the gradient in the phase across each vertex. The goal is to leave only the average phase. The gradient-correction term is computed as the difference of two images; the fitted field, such as in Fig. S7b, and the fitted field with the gradient parameters $\mathbf{g}_i$ set to zero for the local field terms. This correction is applied to the observed image in Fig. S7a to produce the gradient-corrected image in Fig. S7d. The images of ferromagnetic spin configurations in Fig. 2 of the main text have also been subjected to a gauge transformation: A subset of the vertices receive a local π phase shift; see Sec. II F for an explanation.

E. Atomic position calibration

The positions of the atoms are confined to the $z = 0$ midplane of the confocal cavity. In order to locate this position, we do an interferometric measurement of an intracavity lattice injected longitudinally. Specifically, we address the cavity with two different wavelengths separated by an integer multiple Δq of the FSR. The difference in spatial phase between the lattices created with these two wavelengths changes as a function of z as $\Delta q \frac{\pi}{2L}(2z + L)$ and can be measured by a multipulse Kapitza-Dirac measurement.

This kind of measurement relies on accurate knowledge of the longitudinal spatial phase of the intracavity lattice. This is challenging in a confocal cavity, since the longitudinal character depends strongly on the transverse mode content of the light field being injected [35, 36]. Instead, we perform this measurement with the length of the cavity set to a single-mode configuration, where the TEM$_{00}$ mode, which has a known longitudinal spatial phase dependence, can be isolated and addressed. By accounting for the known change in cavity length between this single-mode configuration and the confocal configuration employed in this work, we are then able to position the atoms to within 10 μm of the midplane.

To transversely position the atoms in the $z = 0$ midplane, we rely on the local-field emission of the confocal cavity, which can be imaged with high resolution [11]. We extract the position(s) by fitting the superradiant cavity emission as described in Sec. I D.

F. Data processing

We perform a minimal amount of data processing after fitting the cavity fields to reconstruct the spin state, as described above in Sec. I D. We exclude experimental shots where the fitter does not provide a reasonable set of atomic vertex positions based on approximately known trap positions. This occurs in $\sim 8\%$ of the experimental shots.

Comparing all observed positions to the target positions, we find that the fluctuations in vertex position are distributed as an isotropic Gaussian. The shot-to-shot position fluctuations have a standard deviation of 0.73 μm. This position noise induces a small amount of variance in the quenched disorder in the coupling matrix from shot-to-shot. We estimate the effect of this on the overlap distribution by using simulated-annealing simulations. A set of replicas are cooled down to $\sim 0.05 T_c$ with 0.73 μm standard deviation Gaussian noise added to the atomic positions for each replica. Each replica thus has a slightly different J matrix. The equilibrium overlap distribution between replicas is computed after annealing to low temperature. The overlap distribution with noisy positions is compared to the distribution with no noise. We find a correlation with the noise-free overlap distribution of greater than 90%, averaged over many sets of positions.

For a given position configuration, we require 100 experimental replicas after filtering to produce a sufficiently converged overlap distribution. See Sec. VI for a discussion of convergence of the overlap in terms of the number of replicas. Any additional replicas are discarded to keep constant the number per disorder-instance at exactly 100.

II. CONFOCAL CAVITY QED SPIN MODEL

For simplicity, the atoms in each of the $n = 8$ atomic gas clouds are approximated as being in a BEC, allowing each ensemble to be described by an atomic field operator $\hat{\psi}_i(\mathbf{x})$. After elimination of the atomic excited state, the Hamiltonian is:

$$\hat{H} = -\sum_\mu \Delta_\mu \hat{a}_\mu^\dagger \hat{a}_\mu + \sum_{i=1}^n \hat{H}_{A,i} + \sum_{i=1}^n \hat{H}_{LM,i}, \tag{S3}$$

$$\hat{H}_{A,i} = \int d^3\mathbf{x}\, \hat{\Psi}_i^\dagger(\mathbf{x}) \left(-\frac{\nabla^2}{2m} + V(\mathbf{x}) \right) \hat{\Psi}_i(\mathbf{x}), \tag{S4}$$

$$\hat{H}_{LM,i} = \frac{1}{\Delta_A} \int d^3\mathbf{x}\, \hat{\Psi}_i^\dagger(\mathbf{x}) \hat{\Phi}_T^\dagger(\mathbf{x}) \hat{\Phi}_T(\mathbf{x}) \hat{\Psi}_i(\mathbf{x}). \tag{S5}$$

The individual cavity modes are indexed by μ. The pump detuning is Δ_μ and photon annihilation operators are $\hat{a}_\mu$. The externally applied trapping potential is given by $V(\mathbf{x})$. The trap potential contains 8 minima that define the locations of the vertices of the network. The minima occur at locations $\mathbf{x}_i$ and are anisotropic with trap frequencies $\omega_{x,y,z}$. We neglect s-wave scattering between atoms because it results in only a small shift of the superradiance threshold [56].

The light-matter Hamiltonian $\hat{H}_{LM,i}$ contains the total light field $\hat{\Phi}_T(x) = \Omega \cos(k_r x) + g_0 \hat{\Phi}(x)$. The first term is the standing-wave transverse pump, where the Rabi strength is Ω, $k_r = 2\pi/\lambda$ is the recoil momentum, and λ is the wavelength of the light. The second term contains the total cavity field operator $\hat{\Phi}(\mathbf{x})$; the single-mode, single-photon interaction strength is g_0. The cavity field is expressed in terms of individual modes as

$$\hat{\Phi}(\mathbf{x}) = \sum_\mu \hat{a}_\mu \Xi_\mu(\mathbf{r}) \cos\left(k_r z - \theta_\mu\right). \tag{S6}$$

This expression assumes that $|z|$ is much smaller than the mode's Rayleigh range (5 mm in this confocal cavity), which is satisfied since typical z are less than 10 μm. A mode-dependent phase shift $\theta_\mu = n_\mu \pi/4$ serves to satisfy boundary conditions in the cavity, where $n_\mu = l + m$. The transverse-mode function near the cavity midplane is

$$\Xi_\mu(\mathbf{r}) = H_l\left(\sqrt{2}x/w_0\right) H_m\left(\sqrt{2}y/w_0\right) \exp(-\mathbf{r}^2/w_0^2), \tag{S7}$$

where $H_n(x)$ are the Hermite polynomials. We use $\mathbf{r}$ to denote the in-plane part of the general coordinate $\mathbf{x}$. Only families of modes with all even or all odd n_μ are simultaneously resonant; we focus on an even resonance, and so all sums over μ are implicitly restricted to $n_\mu = 0 \mod 2$. This results in cavity modes that alternate in longitudinal shape between $\cos(k_r z)$ and $\sin(k_r z)$ [35, 36].

The atomic degrees of freedom develop a DW of wavevector k_r at the superradiant transition. This can be described by writing the atomic field operators in a basis containing the DW excitations,

$$\hat{\Psi}_i(\mathbf{x}) = \sqrt{E(\mathbf{x} - \mathbf{x}_i)} \left[\hat{\psi}_{0,i} + 2\hat{\psi}_{c,i} \cos(k_r z)\cos(k_r x) + 2\hat{\psi}_{s,i} \sin(k_r z)\cos(k_r x) \right]. \tag{S8}$$

The operators $\hat{\psi}_{\sigma,i}$, where $\sigma \in \{0, c, s\}$, are independent bosonic modes with canonical commutation relations $[\hat{\psi}_{\sigma,i}, \hat{\psi}_{\tau,j}^\dagger] = \delta_{\sigma\tau}\delta_{ij}$ and $[\hat{\psi}_{\sigma,i}, \hat{\psi}_{\tau,j}] = [\hat{\psi}_{\sigma,i}^\dagger, \hat{\psi}_{\tau,j}^\dagger] = 0$. These operators describe excitations of the BEC ground state, cosine DW, or sine DW, respectively. The envelope function $E(\mathbf{x})$ is assumed to be identical for each vertex. The position of vertex i is $\mathbf{x}_i = (\mathbf{r}_i, z_i)$, where we take all vertices to be in the midplane $z_i = 0$ and $\mathbf{r}_i$ denotes the 2D position in the midplane. Normalization of the field operators is achieved by choosing an envelope function for which $\int d^3\mathbf{x} E(\mathbf{x}) = 1$. We note that this atomic ansatz ignores higher-order corrections involving Mathieu functions that describe organization in a deep lattice [55]. This results in a renormalization of only the superradiant threshold, which is unimportant to this work.

To proceed, we insert the expansion of the atomic fields into Eqs. (S4) and (S5) and evaluate the integrals. We assume that the extent of $E(\mathbf{x})$ is large compared to λ, allowing us to drop fast-oscillating terms. For $\hat{H}_{A,i}$, this results in

$$\hat{H}_{A,i} = 2E_r \left(\hat{\psi}_{c,i}^\dagger \hat{\psi}_{c,i} + \hat{\psi}_{s,i}^\dagger \hat{\psi}_{s,i} \right) + E_{\text{trap},i} \left(\hat{\psi}_{0,i}^\dagger \hat{\psi}_{0,i} + \hat{\psi}_{c,i}^\dagger \hat{\psi}_{c,i} + \hat{\psi}_{s,i}^\dagger \hat{\psi}_{s,i} \right), \tag{S9}$$

where $E_r = \hbar^2 k_r^2/(2m)$ is the recoil energy and $E_{\text{trap},i} = \int d^3\mathbf{x} V(\mathbf{x})E(\mathbf{x} - \mathbf{x}_i)$ is the trap energy. Evaluation of the light-matter coupling produces three terms,

$$\begin{aligned}
\hat{H}_{LM,i} =& \frac{\Omega^2}{2\Delta_A} \left(\hat{\psi}_{0,i}^\dagger \hat{\psi}_{0,i} + \frac{3}{2}\hat{\psi}_{c,i}^\dagger \hat{\psi}_{c,i} + \frac{3}{2}\hat{\psi}_{s,i}^\dagger \hat{\psi}_{s,i} \right) \\
&+ \frac{g_0\Omega}{2\Delta_A}\sum_\mu (\hat{a}_\mu + \hat{a}_\mu^\dagger)\left[\cos(\theta_\mu)\hat{\chi}_{c,i} + \sin(\theta_\mu)\hat{\chi}_{s,i}\right]\int d^2\mathbf{r}\rho(\mathbf{r} - \mathbf{r}_i)\Xi_\mu(\mathbf{r}) \\
&+ \frac{g_0^2}{2\Delta_A}\hat{\psi}_{0,i}^\dagger \hat{\psi}_{0,i}\sum_{\mu,\nu}\hat{a}_\mu^\dagger\hat{a}_\nu \cos(\theta_\mu - \theta_\nu)\int d^2\mathbf{r}\rho(\mathbf{r} - \mathbf{r}_i)\Xi_\mu(\mathbf{r})\Xi_\nu(\mathbf{r}) + O(\hat{a}^\dagger\hat{a}\hat{\psi}_{c/s,i}^\dagger\hat{\psi}_{c/s,i}),
\end{aligned} \tag{S10}$$

where $\hat{\chi}_{c/s,i} = \hat{\psi}_{0,i}\hat{\psi}_{c/s,i}^\dagger + \hat{\psi}_{0,i}^\dagger\hat{\psi}_{c/s,i}$ are Hermitian operators and $\rho(\mathbf{r}) = \int dz E(\mathbf{x})$ is the transverse density profile of the atomic ensemble. The first line describes a pump-induced light shift while the second line describes coupling between the atomic DW and cavity light. The last line describes a multimode dispersive shift due to both the ground-state atomic gas and the DW components. The latter terms are not written out because we ignore the dispersive shift for simplicity in what follows.

The total Hamiltonian has a set of n conserved quantities corresponding to the total number of atoms in each ensemble. The observables $N_i = \hat{\psi}_{0,i}^\dagger\hat{\psi}_{0,i} + \hat{\psi}_{c,i}^\dagger\hat{\psi}_{c,i} + \hat{\psi}_{s,i}^\dagger\hat{\psi}_{s,i}$ correspond to the number of atoms in the i'th vertex and are conserved by $\hat{H}$, leading to the U(1) symmetry of the overall phase of the atomic field $\hat{\Psi}_i(\mathbf{x})$. The system also possesses two independent $\mathbb{Z}_2$ symmetries. The first symmetry corresponds to the transformation $\hat{\psi}_{c,i} \to -\hat{\psi}_{c,i}$ for all i. The other symmetry is identical but for the $\hat{\psi}_{s,i}$ operators. We further discuss the role of these symmetries in Sec. II E.

The photonic degrees of freedom can now be adiabatically eliminated. This approximation is valid in the limit $|\Delta_\mu| \gg \frac{g_0\Omega}{|\Delta_A|}, \frac{Ng_0^2}{|\Delta_A|}, E_r$, where the cavity field dynamics are much faster than the atomic motion. Elimination proceeds by writing the equation of motion for $\hat{a}_\mu$ based on Eqs. (S3), (S9), and (S10) and including cavity dissipation with photon loss rate 2κ. Setting the time derivative to zero yields

$$\hat{a}_\mu = \frac{g_0\Omega}{2\Delta_A(\Delta_\mu + i\kappa)}\sum_{i=1}^n \hat{R}_{\mu,i}\int d^2\mathbf{r}\rho(\mathbf{r} - \mathbf{r}_i)\Xi_\mu(\mathbf{r}), \tag{S11}$$

where we define $\hat{R}_{\mu,i} = \cos(\theta_\mu)\hat{\chi}_{c,i} + \sin(\theta_\mu)\hat{\chi}_{s,i}$. This expression for $\hat{a}_\mu$ is substituted back into the equations of motion for the atomic fields to find an atom-only Hamiltonian with a light-mediated interaction. Up to an overall energy shift, the atom-only Hamiltonian is given by

$$\begin{aligned}
\hat{H}_{\text{atom-only}} =& \left(2E_r + \frac{\Omega^2}{4\Delta_A} \right)\sum_{i=1}^n \left(\hat{\psi}_{c,i}^\dagger\hat{\psi}_{c,i} + \hat{\psi}_{s,i}^\dagger\hat{\psi}_{s,i} \right) \\
&+ \frac{g_0^2\Omega^2}{4\Delta_A^2}\sum_{i,j=1}^n\sum_\mu \frac{\hat{R}_{\mu,i}\hat{R}_{\mu,j}\Delta_\mu}{\Delta_\mu^2 + \kappa^2}\int d^2\mathbf{r}d^2\mathbf{r}'\rho(\mathbf{r} - \mathbf{r}_i)\rho(\mathbf{r}' - \mathbf{r}_j)\Xi_\mu(\mathbf{r})\Xi_\mu(\mathbf{r}').
\end{aligned} \tag{S12}$$

The second line is the light-mediated interaction $\hat{H}_{\text{int}}$, and can be simplified by defining a position-dependent inter-

action function in 2×2 matrix form:

$$\mathcal{D}(\mathbf{r}, \mathbf{r}') = \Delta_C \sum_\mu \frac{\Xi_\mu(\mathbf{r})\Xi_\mu(\mathbf{r}')}{\Delta_\mu + i\kappa} \begin{bmatrix} \cos^2(\theta_\mu) & \cos(\theta_\mu)\sin(\theta_\mu) \\ \cos(\theta_\mu)\sin(\theta_\mu) & \sin^2(\theta_\mu) \end{bmatrix}. \tag{S13}$$

The interaction term can then be written as

$$\hat{H}_{\mathrm{int}} = \frac{g_0^2\Omega^2}{4\Delta_A^2\Delta_C} \sum_{i,j=1}^n \begin{bmatrix} \hat{\chi}_{c,i} \\ \hat{\chi}_{s,i} \end{bmatrix}^\mathsf{T} \int d^2\mathbf{r}\, d^2\mathbf{r}'\, \rho(\mathbf{r} - \mathbf{r}_i)\rho(\mathbf{r}' - \mathbf{r}_j)\,\mathrm{Re}\left[\mathcal{D}(\mathbf{r},\mathbf{r}')\right] \begin{bmatrix} \hat{\chi}_{c,j} \\ \hat{\chi}_{s,j} \end{bmatrix}. \tag{S14}$$

We now evaluate the interaction function $\mathcal{D}$ explicitly using the known Green's function of the harmonic oscillator,

$$G(\mathbf{r}, \mathbf{r}', \varphi) \equiv \sum_\mu \Xi_\mu(\mathbf{r})\Xi_\mu(\mathbf{r}')e^{-n_\mu\varphi} = \frac{e^\varphi}{2\sinh(\varphi)}\exp\left[-\frac{(\mathbf{r}-\mathbf{r}')^2}{2w_0^2\tanh(\varphi/2)} - \frac{(\mathbf{r}+\mathbf{r}')^2}{2w_0^2\coth(\varphi/2)}\right]. \tag{S15}$$

We consider the limit of a perfectly degenerate confocal cavity, for which $\Delta_\mu = \Delta_C$ for all μ. Recalling that we consider an even-parity confocal cavity, for which summations over μ include only modes with $n_\mu = 0 \mod 2$, we find

$$\mathcal{D}(\mathbf{r}, \mathbf{r}') = \frac{1}{2(1 + i\kappa/\Delta_C)}\begin{bmatrix} G^+(\mathbf{r},\mathbf{r}',0) + G^+(\mathbf{r},\mathbf{r}',i\pi/2) & 0 \\ 0 & G^+(\mathbf{r},\mathbf{r}',0) - G^+(\mathbf{r},\mathbf{r}',i\pi/2) \end{bmatrix}, \tag{S16}$$

where $G^+(\mathbf{r},\mathbf{r}',\varphi) = \frac{1}{2}\left[G(\mathbf{r},\mathbf{r}',\varphi) + G(\mathbf{r},-\mathbf{r}',\varphi)\right] = \frac{1}{2}\left[G(\mathbf{r},\mathbf{r}',\varphi) + G(\mathbf{r},\mathbf{r}',\varphi + i\pi)\right]$. This then results in

$$\hat{H}_{\mathrm{int}} = -\sum_{i,j=1}^n \begin{bmatrix} \hat{\chi}_{c,i} \\ \hat{\chi}_{s,i} \end{bmatrix}^\mathsf{T} \begin{bmatrix} J_{ij}^{\mathrm{local}} + J_{ij}^{\mathrm{non}} & 0 \\ 0 & J_{ij}^{\mathrm{local}} - J_{ij}^{\mathrm{non}} \end{bmatrix} \begin{bmatrix} \hat{\chi}_{c,j} \\ \hat{\chi}_{s,j} \end{bmatrix}, \tag{S17}$$

where we have defined the elements of the connectivity matrix as

$$J_{ij}^{\mathrm{local}} = \mathcal{J}\int d^2\mathbf{r}\, d^2\mathbf{r}'\, \rho(\mathbf{r} - \mathbf{r}_i)\rho(\mathbf{r}' - \mathbf{r}_j)G^+(\mathbf{r},\mathbf{r}',0), \tag{S18}$$

$$J_{ij}^{\mathrm{non}} = \mathcal{J}\int d^2\mathbf{r}\, d^2\mathbf{r}'\, \rho(\mathbf{r} - \mathbf{r}_i)\rho(\mathbf{r}' - \mathbf{r}_j)G^+(\mathbf{r},\mathbf{r}',i\pi/2), \tag{S19}$$

and $\mathcal{J} = g_0^2\Omega^2|\Delta_C|/[8\Delta_A^2(\Delta_C^2 + \kappa^2)]$.

We first consider the simplest case in which the atomic distribution is point-like before considering finite-size effects in subsequent sections. The atomic density profiles are then given by $\rho(\mathbf{r} - \mathbf{r}_i) = \delta(\mathbf{r} - \mathbf{r}_i)$. In this case, evaluation of $G^+(\mathbf{r},\mathbf{r}',\varphi)$ in the limit $\varphi \to 0$ results in $\pi\delta\left[(\mathbf{r} - \mathbf{r}')/w_0\right] + \pi\delta\left[(\mathbf{r} + \mathbf{r}')/w_0\right]$. We consider distinct vertex locations $\mathbf{r}_i$ for which the mirror locations also have no overlap, such that $\mathbf{r}_i \neq \pm\mathbf{r}_j$ for $i \neq j$. This yields the simplification $J_{ij}^{\mathrm{local}} = J^{\mathrm{local}}\delta_{ij}$. The nonlocal term takes the form $J_{ij}^{\mathrm{non}} \propto \cos\left(2\mathbf{r}_i \cdot \mathbf{r}_j/w_0^2\right)$ [36]. Thus, the atom-only Hamiltonian takes the form

$$\hat{H}_{\mathrm{atom\text{-}only}} = \left(2E_r + \frac{\Omega^2}{4\Delta_A}\right)\sum_{i=1}^n \left(\hat{\psi}_{c,i}^\dagger\hat{\psi}_{c,i} + \hat{\psi}_{s,i}^\dagger\hat{\psi}_{s,i}\right) - J^{\mathrm{local}}\sum_{i=1}^n \left(\hat{\chi}_{c,i}^2 + \hat{\chi}_{s,i}^2\right) - \sum_{i,j=1}^n J_{ij}^{\mathrm{non}}\left(\hat{\chi}_{c,i}\hat{\chi}_{c,j} - \hat{\chi}_{s,i}\hat{\chi}_{s,j}\right). \tag{S20}$$

The first term imposes an energy cost on the formation of an atomic DW. In the absence of other terms, or at zero pump power, the ground state of the system is thus a BEC with no DW. The second and third terms, which scale with the pump power, represent the light-mediated interaction. Competition between these and the first term drive a transition into the superradiant phase, in which the atoms can organize into a complex pattern of DWs to minimize the energy.

The atom-only Hamiltonian can be recast using Gell-Mann operators to describe the quantum limit of the system. The atomic ansatz in Eq. (S8) approximates each atom as a three-level system, with each atom in either the BEC state or the state with cosine or sine DW modulation. Each atom can thus be represented by the SU(3) Gell-Mann matrices $\{\lambda^k\}$, where $k \in 1,\ldots,8$. Because the atoms within a vertex all couple symmetrically to the rest of the system, the only operators entering into the Hamiltonian are collective sums of Gell-Mann operators. We denote these operators as $\hat{\Lambda}_i^{(k)} \equiv \sum_{j=1}^{N_i} \hat{\lambda}_{ij}^k$, where $\hat{\lambda}_{ij}^k$ is the Gell-Mann operator for the j'th atom in vertex i. The collective Gell-Mann operators $\hat{\Lambda}_i^{(k)}$ satisfy the same commutation relations as the λ^k matrices. The collective Gell-Mann operators

are related to the atomic field operators $= (\hat{\psi}_{0,i}, \hat{\psi}_{c,i}, \hat{\psi}_{s,i})^{\mathsf{T}}$ through the Jordan-Schwinger map $\hat{\Lambda}_i^{(k)} = \hat{\psi}_i^{\mathsf{T}} \lambda^k \hat{\psi}_i$. Performing the map on the atom-only Hamiltonian yields, up to an overall energy shift:

$$\hat{H}_{\text{atom-only}} = -\left(E_r + \frac{\Omega^2}{8\Delta_A}\right) \sum_{i=1}^n \left(\hat{\Lambda}_i^{(3)} + \frac{1}{\sqrt{3}}\hat{\Lambda}_i^{(8)}\right) - \sum_{i=1}^n J_{ii}^{\text{local}} \left[\left(\hat{\Lambda}_i^{(1)}\right)^2 + \left(\hat{\Lambda}_i^{(4)}\right)^2\right] - \sum_{i,j=1}^n J_{ij}^{\text{non}} \left(\hat{\Lambda}_i^{(1)}\hat{\Lambda}_j^{(1)} - \hat{\Lambda}_i^{(4)}\hat{\Lambda}_j^{(4)}\right).$$

$$(S21)$$

Note that the squared operators $(\hat{\Lambda}_i^{(k)})^2$ do not simplify for any $N_i > 1$. The reason is the same as for the case of products of SU(2) collective spin operators. These do not simplify except in the spin-1/2 limit where the spin operators, corresponding to Pauli matrices, form a complete basis.

A. Finite-sized atomic distributions

Two important effects follow from considering the finite size of the atomic distributions. The first is that the interaction matrix changes into a form that normalizes the divergent J^{local} term. Second is that one must account for the possibility that atoms within a vertex adopt a DW whose phase is nonuniform across the vertex. This leads to a new effective coupling term between $\hat{\psi}_{c,i}$ and $\hat{\psi}_{s,j}$ operators.

To account for a spatially dependent DW phase within a vertex, the atomic ansatz is generalized to

$$\hat{\Psi}_i(\mathbf{x}) = \sqrt{E(\mathbf{x} - \mathbf{x}_i)}\left[\hat{\psi}_{0,i} + 2\hat{\psi}_{c,i}\cos[k_r z + \vartheta_i(\mathbf{r})]\cos(k_r x) + 2\hat{\psi}_{s,i}\sin[k_r z + \vartheta_i(\mathbf{r})]\cos(k_r x)\right], \qquad (S22)$$

where $\vartheta_i(\mathbf{r})$ describes the spatial dependence of the DW phase. Derivation of the atom-only Hamiltonian with this modified atomic ansatz proceeds in an identical fashion. An explicit expression for $\hat{H}_{\text{int}}$ can be obtained under the condition that the phase deviation functions $\vartheta_i(\mathbf{r})$ are sufficiently small across the atomic vertices. Specifically, we consider a functional form that contains only the first-order correction, a linear gradient of the phase, using $\vartheta_i(\mathbf{r}) = \mathbf{g}_i \cdot (\mathbf{r} - \mathbf{r}_i)$. In this case, we simplify trigonometric expressions involving $\vartheta_i(\mathbf{r})$ using the small-angle approximations $\cos[\vartheta_i(\mathbf{r})] \approx 1$ and $\sin[\vartheta_i(\mathbf{r})] \approx \mathbf{g}_i \cdot (\mathbf{r} - \mathbf{r}_i)$. We also ignore the contribution of the DW phase gradient to the kinetic energy as it is much smaller than E_r. The interaction Hamiltonian is then

$$\hat{H}_{\text{int}} = -\sum_{i,j=1}^n \begin{bmatrix} \hat{\chi}_{c,i} \\ \hat{\chi}_{s,i} \end{bmatrix}^{\mathsf{T}} \begin{bmatrix} J_{ij}^{\text{local}} + J_{ij}^{\text{non}} & K_{ij} \\ K_{ij} & J_{ij}^{\text{local}} - J_{ij}^{\text{non}} \end{bmatrix} \begin{bmatrix} \hat{\chi}_{c,j} \\ \hat{\chi}_{s,j} \end{bmatrix}, \qquad (S23)$$

where the new symmetric matrix K_{ij} describes a cross-coupling between $\hat{\chi}_c$ and $\hat{\chi}_s$ operators. Within this small-angle approximation, the integral expressions for J_{ij}^{local} and J_{ij}^{non} are unchanged and thus are still given by Eq. (S18) and Eq. (S19), respectively. Elements of the K matrix are given by

$$K_{ij} = \mathcal{J} \int d^2\mathbf{r} d^2\mathbf{r}' \rho(\mathbf{r} - \mathbf{r}_i)\rho(\mathbf{r}' - \mathbf{r}_j) G^+(\mathbf{r}, \mathbf{r}', i\pi/2)\left[\mathbf{g}_i \cdot (\mathbf{r} - \mathbf{r}_i) + \mathbf{g}_j \cdot (\mathbf{r}' - \mathbf{r}_j)\right]. \qquad (S24)$$

This results in an atom-only Hamiltonian given by

$$\hat{H}_{\text{atom-only}} = \left(2E_r + \frac{\Omega^2}{4\Delta_A}\right) \sum_{i=1}^n \left(\hat{\psi}_{c,i}^\dagger \hat{\psi}_{c,i} + \hat{\psi}_{s,i}^\dagger \hat{\psi}_{s,i}\right) - \sum_{i=1}^n J_{ii}^{\text{local}}\left(\hat{\chi}_{c,i}^2 + \hat{\chi}_{s,i}^2\right) \qquad (S25)$$

$$- \sum_{i,j=1}^n J_{ij}^{\text{non}}\left(\hat{\chi}_{c,i}\hat{\chi}_{c,j} - \hat{\chi}_{s,i}\hat{\chi}_{s,j}\right) - \sum_{i,j=1}^n K_{ij}\left(\hat{\chi}_{c,i}\hat{\chi}_{s,j} + \hat{\chi}_{s,i}\hat{\chi}_{c,j}\right).$$

The quantum model, including the new K matrix coupling term, is then derived through the same Jordan-Schwinger mapping. The associated atom-only Hamiltonian is

$$\hat{H}_{\text{atom-only}} = -\left(E_r + \frac{\Omega^2}{8\Delta_A}\right)\sum_{i=1}^n \left(\hat{\Lambda}_i^{(3)} + \frac{1}{\sqrt{3}}\hat{\Lambda}_i^{(8)}\right) - \sum_{i=1}^n J_{ii}^{\text{local}}\left[\left(\hat{\Lambda}_i^{(1)}\right)^2 + \left(\hat{\Lambda}_i^{(4)}\right)^2\right] \qquad (S26)$$

$$- \sum_{i,j=1}^n J_{ij}^{\text{non}}\left(\hat{\Lambda}_i^{(1)}\hat{\Lambda}_j^{(1)} - \hat{\Lambda}_i^{(4)}\hat{\Lambda}_j^{(4)}\right) - \sum_{i,j=1}^n K_{ij}\left(\hat{\Lambda}_i^{(1)}\hat{\Lambda}_j^{(4)} + \hat{\Lambda}_i^{(4)}\hat{\Lambda}_j^{(1)}\right).$$

The integral expressions for the coupling matrices can be exactly evaluated for Gaussian atomic densities $\rho(\mathbf{r}) = \exp(-\mathbf{r}^2/2\sigma_A^2)/(2\pi\sigma_A^2)$. Integration results in the expressions

$$J_{ij}^{\text{local}} = \frac{\mathcal{J}w_0^2}{8\sigma_A^2}\left[\exp\left(-\frac{(\mathbf{r}_i - \mathbf{r}_j)^2}{4\sigma_A^2}\right) + \exp\left(-\frac{(\mathbf{r}_i + \mathbf{r}_j)^2}{4\sigma_A^2}\right)\right], \tag{S27}$$

$$J_{ij}^{\text{non}} = \mathcal{J}\frac{w_0^2}{w_{\text{eff}}^2}\exp\left(-\frac{2\sigma_A^2}{w_{\text{eff}}^2}\frac{\mathbf{r}_i^2 + \mathbf{r}_j^2}{w_0^2}\right)\cos\left(\frac{2\mathbf{r}_i \cdot \mathbf{r}_j}{w_{\text{eff}}^2}\right), \tag{S28}$$

$$K_{ij} = -\frac{2\mathcal{J}\sigma_A^2}{w_{\text{eff}}^2}\exp\left(-\frac{2\sigma_A^2}{w_{\text{eff}}^2}\frac{\mathbf{r}_i^2 + \mathbf{r}_j^2}{w_0^2}\right)$$
$$\times\left[\frac{w_0^2}{w_{\text{eff}}^2}(\mathbf{r}_j \cdot \mathbf{g}_i + \mathbf{r}_i \cdot \mathbf{g}_j)\sin\left(\frac{2\mathbf{r}_i \cdot \mathbf{r}_j}{w_{\text{eff}}^2}\right) + \frac{2\sigma_A^2}{w_{\text{eff}}^2}(\mathbf{r}_i \cdot \mathbf{g}_i + \mathbf{r}_j \cdot \mathbf{g}_j)\cos\left(\frac{2\mathbf{r}_i \cdot \mathbf{r}_j}{w_{\text{eff}}^2}\right)\right], \tag{S29}$$

where $w_{\text{eff}} = w_0\sqrt{1 + 4\sigma_A^4/w_0^4}$. Thus, due to the finite size of the atomic distribution, the J^{local} term is broadened from a delta function for point-like particles, to a distribution with finite width and amplitude. The J^{non} term is less significantly impacted: The finite size of the atomic distribution primarily sets a long-wavelength Gaussian envelope over the nonlocal interaction.

In summary, the finite size of the atomic distribution allows gradients to appear in the DW phase of each vertex. A coarse-grained model is obtained by integrating over the area of the atomic distribution to recover a point-like vertex model at the cost of introducing a new term to the effective energy. This new term, described by the K-matrix, is proportional to the area of the atomic density.

B. Intracavity field

To find the intracavity field, we use the expression for $\hat{a}_\mu$ in the adiabatic approximation. Accounting for the DW phase gradient, this is

$$\hat{a}_\mu = \frac{g_0\Omega}{2\Delta_A(\Delta_\mu + i\kappa)}\sum_{i=1}^{n}\int d^2\mathbf{r}\,(\cos[\theta_\mu + \vartheta_i(\mathbf{r})]\hat{\chi}_{c,i} + \sin[\theta_\mu + \vartheta_i(\mathbf{r})]\hat{\chi}_{s,i})\,\rho(\mathbf{r} - \mathbf{r}_i)\Xi_\mu(\mathbf{r}). \tag{S30}$$

Note the appearance of the phase deviation functions $\vartheta_i(\mathbf{r})$ inside the integral, compared to Eq. (S11). We can then insert this expression into Eq. (S6). Relying on the Green's functions, we have

$$\hat{\Phi}(\mathbf{x}) = \frac{g_0\Omega}{4\Delta_A(\Delta_C + i\kappa)}\sum_i\int d^2\mathbf{r}'\rho(\mathbf{r}' - \mathbf{r}_i)\left[G^+(\mathbf{r},\mathbf{r}',0)\Big(\cos[k_r z + \vartheta_i(\mathbf{r}')]\hat{\chi}_{c,i} + \sin[k_r z + \vartheta_i(\mathbf{r}')]\hat{\chi}_{s,i}\Big)\right.$$
$$\left. + G^+(\mathbf{r},\mathbf{r}',i\pi/2)\Big(\cos[k_r z - \vartheta_i(\mathbf{r}')]\hat{\chi}_{c,i} - \sin[k_r z - \vartheta_i(\mathbf{r}')]\hat{\chi}_{s,i}\Big)\right]. \tag{S31}$$

The light emitted from the cavity on one side, say propagating along $+z$, is the component of the field with spatial dependence $e^{ik_r z}$. This forward-propagating part is

$$\hat{\Phi}^F(\mathbf{r}) = \frac{g_0\Omega}{8\Delta_A(\Delta_C + i\kappa)}\sum_i\left[\Phi_{\text{loc}}(\mathbf{r};\mathbf{r}_i)(\hat{\chi}_{c,i} - i\hat{\chi}_{s,i}) + \Phi_{\text{non}}(\mathbf{r};\mathbf{r}_i)(\hat{\chi}_{c,i} + i\hat{\chi}_{s,i})\right], \tag{S32}$$

where we defined

$$\Phi_{\text{local}}(\mathbf{r};\mathbf{r}_i) = \int d^2\mathbf{r}'\rho(\mathbf{r}' - \mathbf{r}_i)G^+(\mathbf{r},\mathbf{r}',0)e^{i\vartheta_i(\mathbf{r}')}, \tag{S33}$$

$$\Phi_{\text{non}}(\mathbf{r};\mathbf{r}_i) = \int d^2\mathbf{r}'\rho(\mathbf{r}' - \mathbf{r}_i)G^+(\mathbf{r},\mathbf{r}',i\pi/2)e^{-i\vartheta_i(\mathbf{r}')}, \tag{S34}$$

as the local and nonlocal field arising from a source at position $\mathbf{r}_i$ with density distribution ρ. We note that the nonlocal field generated by vertex i, i.e., $\Phi_{\text{non}}(\mathbf{r};\mathbf{r}_i)$, allows one to recover elements of the J and K matrices. To average over the vicinity of $\mathbf{r}_j$, we calculate the integral

$$I_{ij} = \int d^2\mathbf{r}\rho(\mathbf{r} - \mathbf{r}_j)\Phi_{\text{non}}(\mathbf{r};\mathbf{r}_i) = \int d^2\mathbf{r}d^2\mathbf{r}'\rho(\mathbf{r} - \mathbf{r}_i)\rho(\mathbf{r}' - \mathbf{r}_j)G^+(\mathbf{r},\mathbf{r}',i\pi/2)\big[1 - i\mathbf{g}_i \cdot (\mathbf{r} - \mathbf{r}_i)\big], \tag{S35}$$

where we used the linear approximation of $\vartheta_i(\mathbf{r}')$ as well as a small-angle expansion, swapped integration variables, and used $G(\mathbf{r}, \mathbf{r}', \varphi) = G(\mathbf{r}', \mathbf{r}, \varphi)$. By comparing to Eqs. (S19) and (S24), it can thus be seen that $J_{ij}^{\mathrm{non}}/\mathcal{J} = \mathrm{Re}\{I_{ij}\}$ and $K_{ij}/\mathcal{J} = -\mathrm{Im}\{I_{ij} + I_{ji}\}$.

Assuming a Gaussian density and again using the linear approximation for $\vartheta_i(\mathbf{r}') = \mathbf{g}_i \cdot (\mathbf{r}' - \mathbf{r}_i)$, we can explicitly evaluate the local and nonlocal fields as

$$\Phi_{\mathrm{local}}(\mathbf{r}; \mathbf{r}_i) = \frac{w_0^2}{4\sigma_A^2} \left(\exp\left[-\frac{(\mathbf{r} - \mathbf{r}_i)^2}{2\sigma_A^2} + i\mathbf{g}_i \cdot (\mathbf{r} - \mathbf{r}_i) \right] + \exp\left[-\frac{(\mathbf{r} + \mathbf{r}_i)^2}{2\sigma_A^2} - i\mathbf{g}_i \cdot (\mathbf{r} + \mathbf{r}_i) \right] \right), \tag{S36}$$

$$\Phi_{\mathrm{non}}(\mathbf{r}; \mathbf{r}_i) = \exp\left[-\frac{2\mathbf{r}^2 \sigma_A^2}{w_0^4} - \frac{1}{2}\mathbf{g}_i^2 \sigma_A^2 \right] \cos\left[\frac{2}{w_0^2} \mathbf{r} \cdot (\mathbf{r}_i - i\mathbf{g}_i \sigma_A^2) \right]. \tag{S37}$$

C. Discussion of density-wave gradients

Experimentally, we find that the gradients are related to vertex positions via $\mathbf{g}_i = -2\mathbf{r}_i/w_{\mathrm{eff}}^2$. We now discuss this behavior in more detail. The relation between gradient $\mathbf{g}_i$ and vertex position $\mathbf{r}_i$ can be understood for individual vertices as a consequence of the nonlocal superradiant emission pattern that it generates: It is energetically favorable for the DW to adopt a gradient that matches the wavevector of the nonlocal field. A vertex at position $\mathbf{r}_i$, generates a nonlocal field of the form $e^{i\mathbf{k}\cdot\mathbf{r}} + e^{-i\mathbf{k}\cdot\mathbf{r}}$, where the wavevector is $\mathbf{k} = \pm 2\mathbf{r}_i/w_{\mathrm{eff}}^2$. The expression for $\mathbf{g}_i$ matches one of these wavevectors.

For superradiance experiments with multiple vertices, nonlocal fields interfere and the optimal phase evolution across a vertex may differ from this single-vertex optimal gradient. Nonetheless, we experimentally find that the gradients still closely follow this same prediction. We extract the gradients from the full fit as described in Sec. I D. Their magnitude and direction are illustrated in Fig. S8, where we plot the statistics of the entire dataset, i.e., 12,300 experimental shots with 8 atomic vertices each. Figure S8a shows the strong correlation between gradient magnitude and distance from cavity center; the red dashed line is the relation $|\mathbf{g}| = 2|\mathbf{r}|/w_0^2$. To assess the direction of the gradients, we show in Fig. S8b the inner product between gradient and position unit vectors, i.e., the cosine of the angle between the gradient direction and vertex position vector. These are all clustered at -1, indicating that the gradient points toward the cavity center.

Using the above relation between gradient and position, the K-matrix from Eq. (S29) can now be simplified to

$$K_{ij} = \frac{2\mathcal{J}\sigma_A^2}{w_{\mathrm{eff}}^2} \exp\left(-\frac{2\sigma_A^2}{w_{\mathrm{eff}}^2} \frac{\mathbf{r}_i^2 + \mathbf{r}_j^2}{w_0^2} \right) \left[\frac{4w_0^2 \mathbf{r}_i \cdot \mathbf{r}_j}{w_{\mathrm{eff}}^4} \sin\left(\frac{2\mathbf{r}_i \cdot \mathbf{r}_j}{w_{\mathrm{eff}}^2} \right) + \frac{4\sigma_A^2(\mathbf{r}_i^2 + \mathbf{r}_j^2)}{w_{\mathrm{eff}}^4} \cos\left(\frac{2\mathbf{r}_i \cdot \mathbf{r}_j}{w_{\mathrm{eff}}^2} \right) \right]. \tag{S38}$$

The form of this is no longer gradient-dependent. This position-dependent form is used in this work and presented in an approximate form in the main text.

We also performed numerical simulations to verify the formation of phase gradients. Simulated annealing for the semiclassical energy Eq. (S41) is used to probe the ground-state spin configuration. We represent each vertex by an ensemble of 100 individual spins that are spatially distributed within the vertex with standard deviation $\sigma_A = 4\ \mu$m.
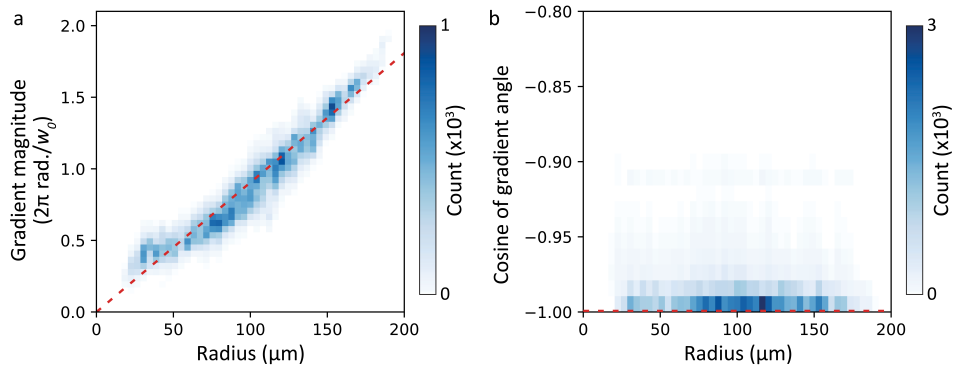

FIG. S8. Observed density-wave gradients. (a) Two-dimensional histogram of observed gradient magnitudes and vertex positions. A strong correlation is observed, closely matching the relation $\mathbf{g} = -2\mathbf{r}/w_0^2$ indicated by the red dashed line. (b) 2D histogram of the gradient directions plotted by taking the cosine of their angle with respect to the position vector. A value of -1 ($+1$) indicates radially inward (outward) pointing gradients.

This method directly probes finite-size effects within a vertex, and so the approximate K-matrix interaction is not used. We verify that gradients develop within the vertices for systems up to at least 8 vertices. In particular, when there is only one vertex, the gradient closely matches the wavevector of the nonlocal field as predicted above. However, for system sizes $n > 1$ we find that the gradient no longer follows this simple prediction, instead forming much less predictable gradients. This can be understood by the fact that the phase gradient now depends on the sum of nonlocal fields from all vertices. Further study is needed to understand the difference between these simulations and experimental observations. Nevertheless, the heuristic model presented above conforms well to our experimental observations.

D. Semiclassical limit

We use a semiclassical description to describe the experimental situation of many atoms per vertex. Each vertex can be described by a 3-component vector (S_i^x, S_i^y, S_i^z). The spin components are defined in terms of expectation values of the atomic field operators, $S_i^x = \langle \hat{\chi}_{c,i} \rangle / N$, $S_i^y = \langle \hat{\chi}_{s,i} \rangle / N$, and $S_i^z = \langle \hat{\psi}_{c,i}^\dagger \hat{\psi}_{c,i} + \hat{\psi}_{s,i}^\dagger \hat{\psi}_{s,i} - \hat{\psi}_{0,i}^\dagger \hat{\psi}_{0,i} \rangle / N$. Normalization of the atomic wavefunction constrains the semiclassical spin vector to lie within the unit sphere. Taking the expectation value of Eq. (S25) and performing a mean-field decoupling of χ operators yields the semiclassical energy

$$E = N \left[2E_r + \frac{\Omega^2}{4\Delta_A} \right] \sum_{i=1}^n S_i^z - N^2 \sum_{i=1}^n J_{ii}^{\text{local}} \left[\left(S_i^x \right)^2 + \left(S_i^y \right)^2 \right] - N^2 \sum_{i,j=1}^n \left[J_{ij}^{\text{non}} \left(S_i^x S_j^x - S_i^y S_j^y \right) + K_{ij} \left(S_i^x S_j^y + S_i^y S_j^x \right) \right]. \tag{S39}$$

Far above the superradiant threshold, the transverse field term $\propto S_i^z$ plays little role and the spin vectors lie near the xy-plane. Approximating the spins as laying fully within the xy-plane allows for a polar coordinate representation $S_i^x = s_i \cos\theta_i$ and $S_i^y = s_i \sin\theta_i$, resulting in a simplified energy

$$E = -N^2 \sum_{i=1}^n J_{ii}^{\text{local}} s_i^2 - N^2 \sum_{i,j=1}^n s_i s_j \left[J_{ij}^{\text{non}} \cos(\theta_i + \theta_j) + K_{ij} \sin(\theta_i + \theta_j) \right]. \tag{S40}$$

Furthermore, the ratio of local-to-nonlocal interaction prefactors are $J^{\text{local}}/J^{\text{non}} \approx 10$, using the observed $\sigma_A \approx 4 \ \mu$m. The interaction energy is thus dominated by the local energy, which ensures that the length of each spin vector is maximized, $s_i = 1$. We can then use an angle-only model

$$E = -N^2 \sum_{i,j=1}^n \left[J_{ij}^{\text{non}} \cos(\theta_i + \theta_j) + K_{ij} \sin(\theta_i + \theta_j) \right]. \tag{S41}$$

This is equivalent to Eq. (1) of the main text after a rewriting using spin components S^x and S^y and the dropping of the superscript on J_{ij}^{non} for simplicity. In the main text we define $J_0 \equiv N^2 \mathcal{J}$ and omit the negligible contribution from κ.

The expression for the semiclassical intracavity field follows from Eq. (S32), with the above substitutions, and results in

$$\Phi^F(\mathbf{r}) = \frac{N g_0 \Omega}{8\Delta_A(\Delta_C + i\kappa)} \sum_i s_i \left[\Phi_{\text{local}}(\mathbf{r}; \mathbf{r}_i) e^{-i\theta_i} + \Phi_{\text{non}}(\mathbf{r}; \mathbf{r}_i) e^{i\theta_i} \right]. \tag{S42}$$

Hence it is clear that the information about the DW phase θ_i for each atomic vertex is encoded in the light-field we detect using holographic imaging.

We verify that the spin vectors indeed lie close to the xy-plane at the equator through numerical simulations. Equilibrium distributions of the semiclassical energy in Eq. (S39) are simulated via parallel-tempering Monte Carlo. The simulation uses vertex positions and widths identical to those measured in the experiment to generate J_{ii}^{local}, J_{ij}^{non}, and K_{ij}. Within the semiclassical approximation, we find the superradiant threshold by performing a linear stability analysis of the normal phase. This becomes classically unstable when $\frac{1}{N}\left[2E_r + \frac{\Omega^2}{4\Delta_A} \right] < \max_i \lambda_i$, where λ_i are the eigenvalues of the block matrix:

$$M = \begin{bmatrix} J^{\text{local}} + J^{\text{non}} & K \\ K & J^{\text{local}} - J^{\text{non}} \end{bmatrix}. \tag{S43}$$

We assume a pump power ($\propto \Omega^2$) that is a factor 1.25 above the critical coupling strength for the superradiant transition. The radius of spins in their equilibrium states is recorded at a temperature of $0.03 \times \max_i \lambda_i$. We find that the average total spin radius is ≥ 0.97 with a standard deviation $\leq 3.7\%$ across an ensemble of disorder realizations. This implies that the spins are close to the boundary of the unit sphere. Additionally, the average radius in the xy-plane ranges between 0.87 and 0.94 across disorder realizations, with a standard deviation $\leq 6.7\%$. Other than a global rescaling, we can therefore approximate $s_i \approx 1$ for all i, which implies that approximating the semiclassical energy expression with the angle-only model is valid in this regime.

Finally, we discuss two additional terms that could be added to this energy. One could introduce a 780-nm intracavity field via longitudinal pumping of the cavity. Use of a digital micromirror device or spatial light modulator enables phase-sensitive local addressing of vertices; the former was demonstrated in [55]. This would result in an energy term corresponding to that of a local longitudinal field,

$$E_{\text{longitudinal}} = \sum_{i=1}^{n} h_i \cos(\theta_i - \phi_i), \tag{S44}$$

where h_i is the effective field strength and ϕ_i is the spatial phase of the driven intracavity light. This would enable the measurement of magnetic susceptibilities. Additionally, a 1560-nm longitudinal probe would result in an optical potential for the DWs that corresponds to an easy-axis term

$$E_{\text{easy-axis}} = \sum_{i=1}^{n} f_i \cos^2(\theta_i - \varphi_i), \tag{S45}$$

where f_i is the easy-axis strength and φ_i its direction.

E. $\mathbb{Z}_2$ symmetries

The effective energy in Eq. (S40) possesses a global $\mathbb{Z}_2$ symmetry; we now describe its effect on the overlaps. For brevity, we denote the configuration of all spins together as $\theta = \{\theta_i\}$. The transformation $\theta \to \theta + \pi$ leaves the energy invariant. As in other superradiance experiments [34], this symmetry is spontaneously broken at the superradiant phase transition. Experimental evidence for this in the spin network is presented in the next section. To understand how this transforms the overlap parameter, we can apply this global Ising spin-flip on replica α but not on replica β. Then, in terms of Q, R, the linear combinations of overlaps matrices defined in the main text, the Ising symmetry results in $(Q, R) \to (-Q, -R)$. This implies that the overlap distributions are symmetric under a 180 degree rotation.

Before considering finite-size effects in Sec. II A, we noted two independent $\mathbb{Z}_2$ symmetries, $\hat{\psi}_{c,i} \to -\hat{\psi}_{c,i}$ and $\hat{\psi}_{s,i} \to -\hat{\psi}_{s,i}$ (for all i). The joint transformation corresponds to the Ising symmetry discussed above. Applying the transformation of only the sine component results in $\theta \to -\theta$ for the semiclassical spin configuration. Physically, this corresponds to the reflection of the DWs in the cavity midplane $z = 0$. The resulting transformation on the overlap parameters can again be understood by applying this operation on only one replica. This results in $(Q, R) \to (R, Q)$, i.e., a reflection of the overlap distribution along the diagonal. This symmetry is missing in the observed spin overlap distributions, except in rare cases such as Fig. 4c of the main text (see also Sec. X). Indeed, the finite-size Hamiltonian Eq. (S25) [or its semiclassical equivalent Eq. (S39)] is not invariant under this transformation. The symmetry is explicitly broken by the choice of DW gradients $\mathbf{g}_i$. In principal, both $\pm \mathbf{g}_i$ configurations should lead to low-energy states. In practice we find only one of these sets, as discussed in Sec. II C. Potential reasons for this symmetry-breaking are the residual ~ 10-μm displacement of the atoms from the cavity midplane, remnant cavity mode dispersion, cavity mirror aberrations, or nonlinearities arising from the imaging readout [36]. The 1560-nm light used to stabilize the cavity length could also introduce a bias via the easy-axis term it induces.

F. Local gauge rotations

We can also consider what happens if we apply the Ising transformation discussed above to only a single spin: $\theta \to \theta + \pi e_i$, where e_i is the i'th unit vector. This is a local transformation of spin i that, by itself, does not leave the energy invariant. This can become a local gauge transformation that leaves the energy invariant by making a corresponding change on the J- and K-matrices, specifically by flipping the sign of each element in the i'th row as well as in the i'th column. The signs of the diagonal elements J_{ii} and K_{ii} are thus flipped twice and remain the same. These local gauge transformations can be applied to transform a staggered ferromagnet into a conventional one and vice versa, leaving the energy landscape invariant.
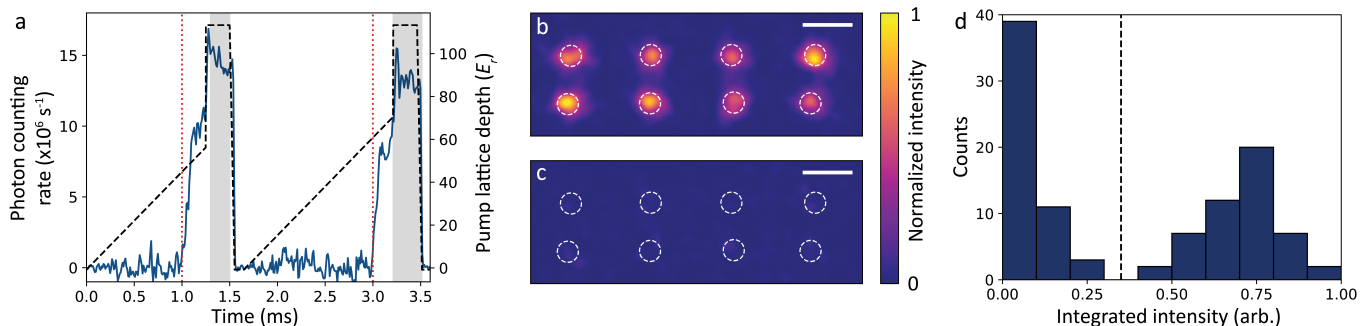
FIG. S9. Experimental evidence for the presence of a $\mathbb{Z}_2$ Ising symmetry. (a) Plot of the double ramp sequence accompanied by a typical cavity emission record. The pump power (dashed black line, right axis) is ramped through the superradiant transition twice, with two readout periods shown by gray regions where the pump is rapidly increased to high power. A typical cavity emission pattern (blue, left axis) shows two superradiant emissions with the superradiant thresholds demarcated by red dashed lines. (b) An example intensity profile of a holographic image in which constructive interference between the two superradiant emissions occurred. (c) An example intensity profile in which destructive interference occurred. Panels (b,c) are shown on the same color scale. (d) The interference signal is derived by integrating the field intensity within the white dashed circular regions of panels (b,c). Histogram of the integrated intensities of 103 experimental cycles. A dashed line at 0.33 separates populations corresponding to constructive and destructive interference.

III.   EXPERIMENTAL VERIFICATION OF $\mathbb{Z}_2$ SYMMETRY

As discussed in Sec. II E, the system contains a $\mathbb{Z}_2$ Ising symmetry in which the spin state θ may be transformed into $\theta + \pi$. Unfortunately, it is not possible to distinguish between these two states from a single holographic image, due to the following reasons. The confocal field in Eq. (S2) is invariant under the joint transformation $\theta \to \theta + \pi$ and $\phi \to \phi + \pi$, where ϕ is phase of the LO beam with respect to the cavity emission. While ϕ is stable over the course of a single experiment, it is not stable from shot to shot, and thus the two $\mathbf{Z}_2$ related states cannot be distinguished using the readout method described in Sec. I D.

Nevertheless, we are able to perform an independent set of experiments that demonstrate the existence of this Ising symmetry. As in earlier work [57–59], the long-term phase fluctuations of the LO can be circumvented by repeatedly ramping in and out of the superradiant phase within a single experimental shot. We accomplish this using the ramp schedule shown in Fig. S9a. This is shown together with a typical cavity emission for a configuration of vertices resulting in a yFM. We change the cavity detuning to $\Delta_C/2\pi = -40$ MHz to enhance the signal strength for these types of experiments. This change is sufficiently small as to not affect the ferromagnetic behavior of this configuration: Indeed, only two global minima oriented along $\theta_i = \pm\pi/2$ are commonly found. To demonstrate this discrete symmetry, two ramps and readout periods follow in close succession, with two superradiant emissions separated by approximately 2 ms. The ramp rate is kept the same as described in the main text, while the ramp durations are optimized to balance the integrated intensity of the two superradiant emissions.

We highlight the use of holographic imaging, rather than temporal heterodyne, to observing spontaneous $\mathbb{Z}_2$-symmetry breaking. This differs from earlier experiments [57–59] and works in the following manner. Holographic fringes from interference between the cavity emission and the LO beam accumulate only during the readout periods, shown as the gray regions in Fig. S9a. The camera is exposed during the full ramp sequence, which allows these two holograms to interfere on the camera. The LO phase is sufficiently stable over this short period to allow an interference signal to develop. If the Ising symmetry is broken spontaneously at the superradiant phase transition, then the phases of the two pulses would be completely independent. The yFM states of opposite $\mathbb{Z}_2$ symmetry would produce cavity emission patterns π out of phase with each other. Thus, the two sequential holograms are equally likely to constructively or destructively interfere. Indeed, we observe both constructive and destructive interference patterns as expected from the Ising symmetry. Figures S9b,c show normalized intensity profiles of the cavity emission for two independent repetitions of the experiment, where Fig. S9b (Fig. S9c) demonstrates fully constructive (destructive) interference.

The probability for realizing constructive or destructive interference is measured over 103 independent repetitions of the experiment. To quantify the level of interference in an image, the intensity of the total field at the location of the vertices is integrated. The regions of integration are demarcated by dashed circles in Figs. S9b,c. The histogram of integrated intensity over all experiments is shown in Fig. S9d. A value of zero corresponds to fully destructive interference; the integrated intensity is normalized by the largest value measured. Two distinct populations are found, corresponding to constructive and destructive interference. Separating the two populations at a value of 0.33 results
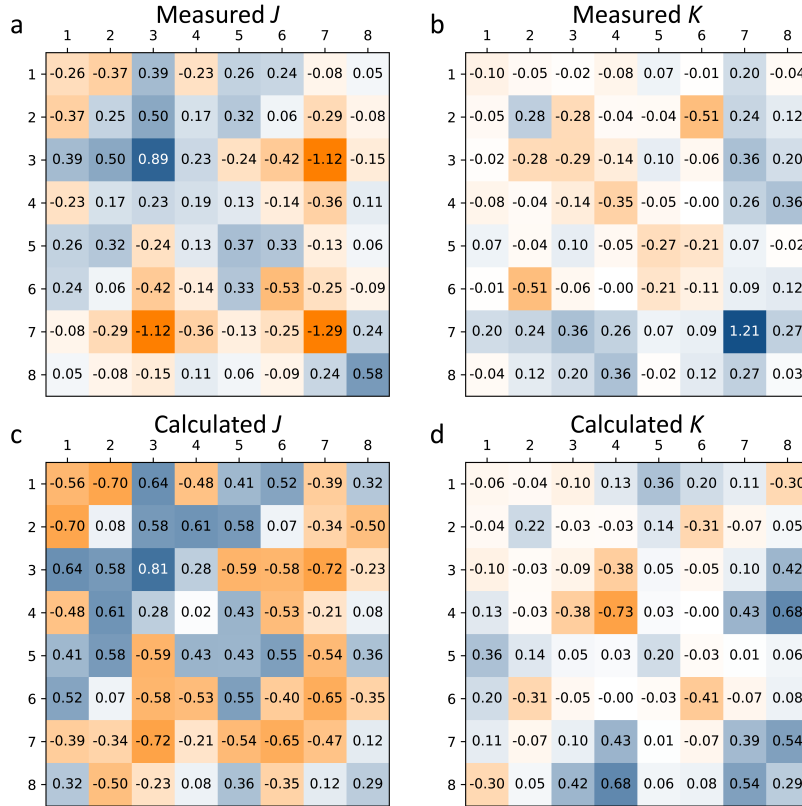
FIG. S10. Comparison between measured and calculated interaction matrices. (a,b) Measured J and K matrices, respectively. (c,d) J and K matrices, respectively, calculated using Eqs. (S28) and (S38) based on vertex position data and measured width of the vertices. Color scale is the real part of the color scheme in Fig. 1c of the main text.

in 48.5% (51.5%) of experiments realizing constructive (destructive) interference. This is in close agreement with the 50% probability expected from spontaneously breaking the Ising symmetry. Because our hologram measurements are not sensitive to the way this symmetry is broken in the experiment, all overlap and magnetization distributions shown in the main text are explicitly symmetrized for clarity.

IV. MEASUREMENT OF THE J AND K-MATRICES

The J and K matrices can be calculated based on the positions $\mathbf{r}_i$ of the atomic vertices in a perfect confocal cavity; see Eqs. (S28) and (S38). We also independently measure these matrices, as discussed in this section, to assess deviations from the calculated matrices due to cavity imperfections. The measurement procedure is as follows. For a given position configuration, we isolate a single vertex i, as described in Sec. I A. Then we perform a superradiance experiment using only this single vertex and record the intracavity field using holographic imaging. This reveals the intracavity field generated by vertex i, which we denote $E_i(\mathbf{r})$. Since the interactions are photon-mediated, this directly provides the interaction coupling strength via the theory presented in Sec. II B. A vertex at position $\mathbf{r}_j$ experiences total interaction $E_i(\mathbf{r}_j)$; note that we actually take a Gaussian average around $\mathbf{r}_j$ to account for the finite vertex width σ_A. The elements J_{ij} and K_{ij} correspond to the real and imaginary part of this quantity, respectively. The recorded cavity field thus provides the entire i'th row of both J and K matrices.

To reduce imaging noise when performing these interaction matrix calibrations, we average together the fields from approximately 30 repetitions of the same superradiance experiment. Repeating this procedure for each vertex provides the values of independent rows of the J and K matrices. We rescale these rows because the brightness of the hologram is not consistent across the vertex positions: Using the fact that the J and K matrices are symmetric, this rescaling is performed by algorithmically minimizing $\|J - J^{\mathsf{T}}\|/\|J\|$. The same rescaling is used for both J and K matrices, and the antisymmetric part of the resulting matrices is discarded.

This measurement process is very time consuming, so we perform this measurement for only a few selected position configurations. Namely, the two ferromagnetic configurations presented in Fig. 2, as well as the disorder instances in

Fig. 3 and Figs. 4a–d. We find good overall agreement between the measured J and K matrices and those calculated from Eqs. (S28) and (S38). Figure S10 presents a direct comparison for the position configuration of Fig. 3 of the main text. The measured matrices can be determined up to only a global rescaling. In Fig. S10, this scale is chosen to maximize the similarity between the experimental and calculated J matrix. We reiterate that the calculated matrices assume perfect confocality, which in practice is hampered by, e.g., astigmatism and mirror surface defects [51].

V. EQUILIBRIUM AND NONEQUILIBRIUM NUMERICAL SIMULATIONS

We use parallel-tempering Monte Carlo simulations [46] to study equilibrium properties of our system. The simulations follow the even/odd deterministic swapping algorithm [60, 61], typically with 10 geometrically sampled temperatures ranging from $\sim 0.05T_c$ to $2T_c$. States are sampled from the angle-only energy model Eq. (S41) to yield equilibrium overlap and magnetization distributions. We typically use 16,000 update steps to evolve a replica at each temperature, each with a local Gaussian proposal function of standard deviation $\pi/8$. We find that this is sufficient to achieve convergence of the overlap distribution for the $n = 8$ system size.

As discussed in the main text, the parallel-tempering simulations fail to accurately match experimental spin overlap distributions. This is illustrated in Fig. S11(a-l), where we simulate two of the experimentally realized disorder instances using the measured J and K matrix. We show a temperature progression from the paramagnetic phase into an ordered phase. At no temperature does the overlap look comparable to that experimentally observed in Figs. 3 and 4c of the main text. Likewise, the parallel-tempering simulation shown in Fig. S11m–r for the Parisi distribution lacks key features exhibited by the experimentally found distribution in Fig. 4e.
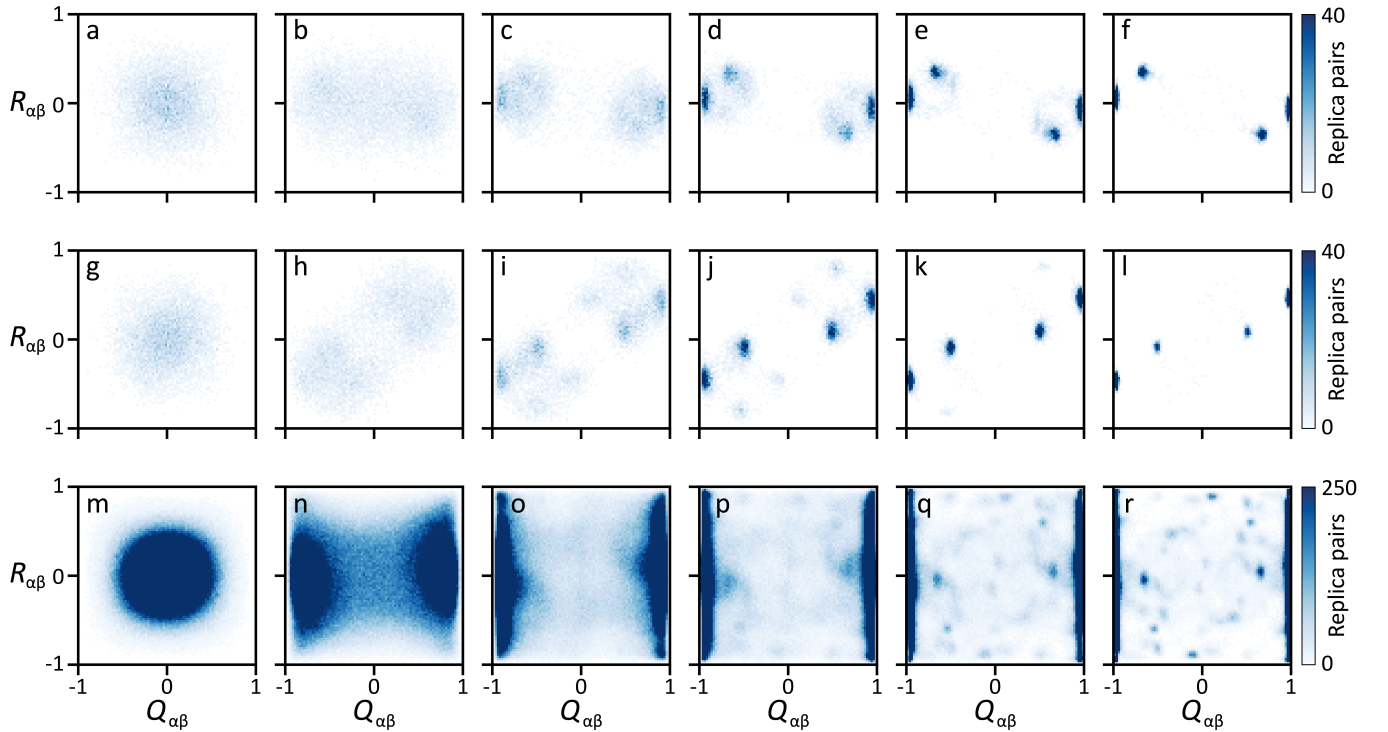

FIG. S11. Equilibrium overlap distributions from parallel tempering. (a-f) Numerical spin overlaps for the disorder instance of Fig. 3 (and Fig. 4a) of the main text. (g-l) Numerical spin overlaps for the disorder instance of Fig. 4c of the main text. (m-r) Numerical Parisi order parameter, disorder averaged over all 123 disorder instances of Fig. 4e of the main text. The temperatures, normalized to the maximum magnitude eigenvalue of the (measured) J matrix $\lambda_{\max}$, are: (a,g,m), 1.11; (b,h,n), 0.34; (c,i,o), 0.19; (d,j,p), 0.11; (e,k,q), 0.06; and (f,l,r), 0.03.

While parallel-tempering simulations provide insight into equilibrium properties, our experiment is manifestly nonequilibrium. Some nonequilibrium effects can be captured through rapid simulated annealing. An initially hot system is simulated under the Metropolis-Hastings algorithm [62, 63] at a temperature T that is rapidly decreased far below T_c. The simulation is stopped before the system is allowed the thermalize. Specifically, we ramp to a final temperature of $0.04T_c$ and perform 560 Metropolis steps per random initial state. For Fig. 4f–i, we use 1000 initial

states to construct the overlap distribution, while Fig. 4j uses 250 initial states for each of the 123 disorder instances.

VI.   BOOTSTRAP ERROR ANALYSIS

The statistical error in magnetization and overlap distributions incurred from having a finite number of experimental replicas is estimated using a bootstrap analysis. We focus here on the overlap distributions; analysis of the magnetization distributions follows identically. Bootstrap samples for a given disorder realization of the J and K matrices are generated by sampling with replacement from the set of measured spin states. The size of the bootstrap sample is equal to the number of measured replica spin states; 900 replicas for the ferromagnetic data in Fig. 2 or 100 replicas per J matrix for the data in Figs. 3 and 4. We then compute the 2D overlap distribution $p_J^{(k)}(Q, R)$ of that bootstrap sample to arrive at a bootstrapped distribution, where k indexes the bootstrap samples. This distribution is compared to the overlap distribution $p_J(Q, R)$ generated directly from the measured set of replicas. Fluctuations in the distributions $p_J^{(k)}(Q, R)$ from one bootstrap sample k to the next are used to determine a bootstrap error estimate on the measured distribution $p_J(Q, R)$. We use 100 bootstrap samples in the results that follow.

A quantitative error estimate is generated using the Hellinger distance between the measured and bootstrapped overlap distributions. The Hellinger distance is

$$d^{(k)} = 1 - \sum_{Q,R} \sqrt{p_J(Q, R)p_J^{(k)}(Q, R)}, \tag{S46}$$

and is zero for identical, normalized distributions, and one for completely nonoverlapping distributions. This distance thus represents a fractional difference between the measured and bootstrapped overlap distributions. Hellinger distances depend on the number of bins in the distribution. Choosing a larger number of bins requires a greater number of measured replicas to achieve the same level of convergence to the large-system-size limit. We choose to use 80 bins per dimension for all overlap and magnetization distributions. This results in an estimated average convergence to within 5% for the measured overlap distributions in Figs. 3 and 4, with a standard deviation of two percentage points over all $N_J = 123$ disorder realizations of the J matrix. The two ferromagnetic systems in Fig. 2, each with 900 replicas, are both estimated to have converged within 4% of their overlap distributions and 2% of their magnetization distributions.

Bootstrap analysis is also used to estimate the convergence of the aggregate overlap and magnetization distributions. While the distributions converge in the limit of many disorder realizations, our experimental ensemble contains a finite number of such realizations. The measured aggregate distribution in Fig. 4e of the main text is constructed to be the average over disorder realizations, $p(Q, R) = \sum_{i=1}^{N_J} p_{J_i}(Q, R)/N_J$. A bootstrap sample can be constructed by sampling with replacement N_J times from the collection of $p_{J_i}(Q, R)$ distributions. That is, a bootstrap sample is generated from a random sample B_k of size N_J that contains possibly repeated disorder realization indices. The bootstrapped aggregate distribution is then constructed as $p^{(k)}(Q, R) = \sum_{i \in B_k} p_{J_i}(Q, R)/N_J$. Fluctuations in the $p^{(k)}(Q, R)$ distributions between bootstrap samples k now indicate the level of convergence in the measured aggregate distribution. The Hellinger distance between measured $p(Q, R)$ and bootstrapped $p^{(k)}(Q, R)$ distributions is again used to extract a metric of convergence. We find that the aggregate overlap distribution of Fig. 4e is estimated to have converged to within 2% of the distribution corresponding to an average over all possible disorder realizations. Similarly, the aggregate magnetization is estimated to be within 3% of the full disorder-averaged distribution.

VII.   EFFECTIVE TEMPERATURE FOR FERROMAGNETIC DATA

The effective temperatures for the ferromagnetic systems shown in Fig. 2 of the main text are found via a Maxwell-Boltzmann fit using the simplified interaction energy in Eq. (S41). These are normalized using an estimated critical temperature T_c. We first describe the form of the Maxwell-Boltzmann distribution used for the fit before describing how T_c is estimated from equilibrium numerical methods.

A.   Derivation of Maxwell-Boltzmann distribution

The Maxwell-Boltzmann distributions for the ferromagnetic systems are amenable to a low-temperature analysis by local expansion around its two (spin-flip-symmetry-related) basins of attraction in the free-energy landscape. We now

derive its generic form by considering the density of states near these global minima. Taylor expansion of Eq. (S41) near the global minimum configuration θ_0 leads to

$$E(\theta_0 + \epsilon) = E_{\text{gs}} + \epsilon^\intercal H \epsilon + O(\epsilon^3), \tag{S47}$$

where $E_{\text{gs}} = E(\theta_0)$ is the ground state energy, and H is the Hessian matrix evaluated at θ_0. This expansion is valid in proximity to the ground state, where $|\epsilon| \ll 1$. This condition is satisfied when the temperature T of the Maxwell-Boltzmann distribution is sufficiently small so that states far from the ground state are not populated.

We now calculate the density of states at a fixed energy level for a general n-vertex spin network system described by Eq. (S47). Integration over the configuration space at a given energy E yields

$$g(E) = \int \delta\left(E - E_{\text{gs}} - \epsilon^\intercal H \epsilon\right) d^n\epsilon = \frac{(E - E_{\text{gs}})^{n/2-1}}{\sqrt{\det(H)}} \int \delta\left(1 - u^\intercal u\right) d^n u, \tag{S48}$$

where we used the fact that the Hessian is a positive definite matrix to perform a change of the integration variable. The resulting integral calculates the surface area of an n-dimensional unit sphere, which is

$$\int \delta\left(1 - u^\intercal u\right) d^n u = \frac{2\pi^{n/2}}{\Gamma(n/2)}. \tag{S49}$$

The density of states is thus given by

$$g(E) = \frac{2}{\Gamma(n/2)} \sqrt{\frac{\pi^n}{\det(H)}} (E - E_{\text{gs}})^{n/2-1}. \tag{S50}$$

The Maxwell-Boltzmann distribution at temperature T is now found by weighting the density of states by the associated Boltzmann-factor and normalizing the distribution:

$$f(E, T) = \frac{(E - E_{\text{gs}})^{n/2-1}}{\Gamma(n/2)T^{n/2}} e^{-(E-E_{\text{gs}})/T}. \tag{S51}$$

This is the functional form used in the fits of Fig. 2 of the main text to extract the temperature of the ferromagnetic systems.

B. Estimation of the ferromagnetic T_c

The critical temperature of the paramagnet-to-ferromagnet transition is estimated via parallel-tempering Monte Carlo using the energy in Eq. (S41). We compute the average absolute m^x and m^y magnetizations after the local
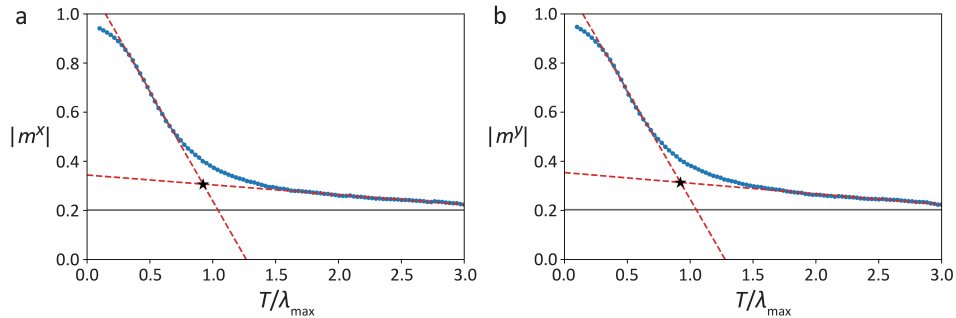

FIG. S12. Estimation of T_c for finite-sized xFM and yFM systems. (a) The absolute magnetization for the xFM state as a function of temperature is found via parallel-tempering simulations. The temperature is normalized to the maximum magnitude eigenvalue of the measured J matrix, λ_{max}. Two separate linear, least-squares fits are performed in the regions $T/\lambda_{\text{max}} = [0.4, 0.7]$ and $[1.5, 3]$, shown as red dashed lines. Their intersection, marked by a star, yields an estimated $T_c = 0.92 \cdot \lambda_{\text{max}}$. The gray horizontal line shows the remnant magnetization $\propto 1/\sqrt{n}$ found in the paramagnetic phase for our finite-size system. (b) The same analysis applied to the yFM system also yields the estimate $T_c = 0.92 \cdot \lambda_{\text{max}}$ in terms of the maximum eigenvalue of the measured yFM J matrix.
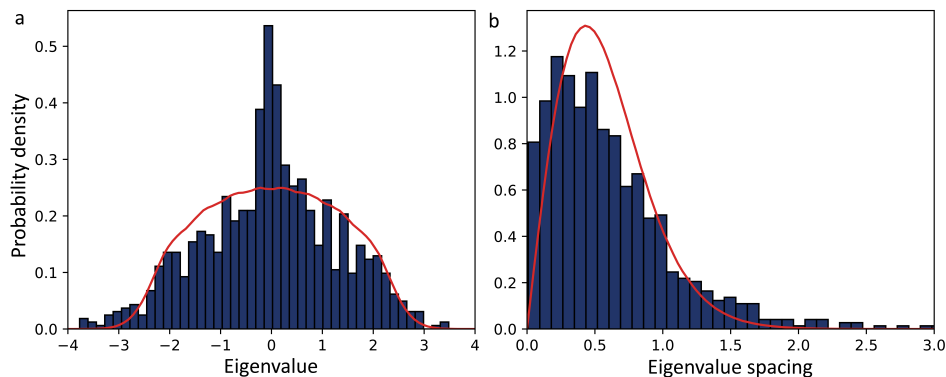
FIG. S13. Experimental ensemble of interaction matrices. (a) Eigenvalue spectrum and (b) level-spacing statistics for the J-matrices calculated from the observed position configurations. Red lines show the expected results for a fully random ensemble, corresponding to $n = 8$ finite-size versions of the Wigner semicircle and Wigner surmise, respectively.

gauge transformations described in Sec. II F. The magnetizations serve as an order parameter as the temperature is varied. A nonanalytic kink in the magnetization occurs at T_c in the thermodynamic limit. For our finite-size system, there is only a crossover region between two approximately linear regimes. We estimate the crossover temperature T_c by performing linear fits on either side of the crossover region and finding the intersection point of the fit results. This would occur at T_c in the large-n limit. The fit results in Fig. S12 show that both the xFM and yFM have an estimated crossover temperature $T_c = 0.92\lambda_{\max}$, where $\lambda_{\max}$ is the magnitude of the eigenvalue of the measured J^{non} matrix with largest absolute value. The dependence on the maximum eigenvalue is standard for mean-field models [64], as this eigenvalue sets the overall energy scale. The appearance of the absolute value reflects the interaction form $S_i^x S_j^x - S_i^y S_j^y$: For yFM there is an additional minus sign which must be taken into account. We conservatively estimate 10% uncertainty in this estimate of T_c, accounting for the fact that this is a crossover. The error reported in T/T_c in the main text is a combination of this uncertainty in T_c and the fit uncertainty of T. Mapping out the full phase diagram of this vector spin model in the thermodynamic limit, including its spin glass phase and potentially mixed phases, will be the subject of future work.

VIII. EXPERIMENTAL ENSEMBLE OF J-MATRICES

We now discuss the ensemble of J-matrices used for the disorder average in Fig. 4e. First, we ensure no two J-matrices are identical. Since the J (and K) matrices are functions of vertex position, we directly compare position configurations between disorder instances. As long as at least one vertex location is different between configurations, the resulting J matrices will be distinct. For each pair of configurations we thus find the most displaced vertex and note its displacement. Across all configuration pairs, these displacements are larger than 4.5 μm$> \sigma_A$. This shows that none of the disorder realizations are identical.

To assess the randomness of the ensemble, we calculate the eigenvalue spectrum and level-spacing distribution for the ensemble of interaction matrices. These are shown in Fig. S13, together with an 8-by-8 symmetric Gaussian orthogonal ensemble for comparison. The experimental ensemble is close to fully random, with the most notable feature being an over-representation of eigenvalues near zero. This is a feature of the confocal cavity interaction, see Ref. [13] for an in-depth study.

IX. QUANTITATIVE ANALYSIS OF ULTRAMETRICITY

To provide evidence for emergent ultrametricity, we analyze the configuration-space structure of the experimental ensemble of states. For ultrametric spaces, the *strong* triangle inequality holds: $D_{\alpha\beta} \leq \max\{D_{\alpha\gamma}, D_{\beta,\gamma}\}$ for all α, β, γ. This can be quantitatively assessed by calculating the $\mathcal{K}$-correlator [45], which is defined for any triplet of replicas as $\mathcal{K} = (D_{\max} - D_{\mathrm{med}})/\sigma(D)$, where $D_{\max(\mathrm{med})}$ is the maximum (median) of the three distances between replicas, and $\sigma(D)$ is the standard deviation of the distribution of all distances. For an ultrametric space, the probability distribution of this correlator is $p(\mathcal{K}) = \delta(\mathcal{K})$. Finite-system sizes introduce some probability for finding small but nonzero values of $\mathcal{K}$, and ultrametricity in such systems has been studied by performing system-size scaling [45, 65].
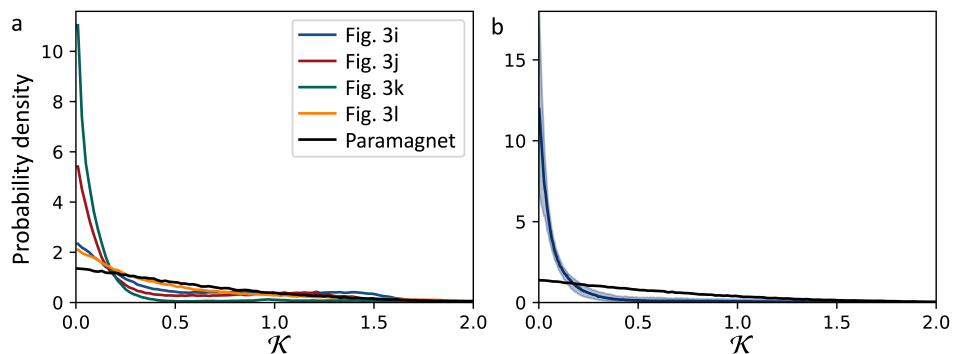
FIG. S14. Quantitative analysis of ultrametric structure. (a) Probability distribution for the $\mathcal{K}$-correlator for the ensembles in Fig. 3 of the main text. A paramagnetic (non-ultrametric) ensemble is shown for comparison. (b) Average probability distribution for the $\mathcal{K}$-correlator across all disorder instances. The shaded area indicates the interquartile range around the median (solid line).

Figure S14a presents the probability distributions for the experimental ensembles in Fig. 3 of the main text. All triplets of replicas are included in the distribution. As a reference for finite-system-size effects, we show $p(\mathcal{K})$ for a paramagnet, i.e., a phase where each state is completely random, sampling 100 states. For the fastest ramp (blue) the system is at high temperature and the distribution is qualitatively comparable to that of the paramagnet. For intermediate ramp rates (red and green) we observe a drastic departure from paramagnetic behavior: The distribution is much stronger peaked at zero, and values of $\mathcal{K}$ greater than 0.5 are significantly suppressed. The slowest, and hence coldest, ensemble (orange) is a single thermodynamic state. Because it does not sample much of the configuration space, its $p(\mathcal{K})$ looks like a paramagnet's. As a single figure-of-merit, we quote the mean $\langle \mathcal{K} \rangle$: This is 0.57 for the paramagnet, and (i) 0.56, (j) 0.39, (k) 0.16, and (l) 0.63 for the experimental ensembles in those panels of Fig. 3.

We perform a similar analysis of all 123 disorder instances included in this work. To show the aggregate behavior, Fig. S14b plots the median (solid blue line) and the interquartile range (shaded area) across all probability distributions. Again the paramagnet is shown for comparison (black line), highlighting the departure of our experimental ensembles from that state with no ultrametric structure. The mean of $\mathcal{K}$ is $\langle \mathcal{K} \rangle = 0.22$, with a standard deviation of 0.14 over the different disorder instances (cf. the paramagnetic value of $\langle \mathcal{K} \rangle = 0.57$).

X. COMPREHENSIVE SET OF SPIN OVERLAPS

Figure 4e of the main text presents the experimental Parisi order parameter distribution from 123 disorder instances. The spin-overlap distribution for each of these instances is shown in Fig. S15. Of these, panels 1 through 4 are presented in the main text as Figs. 4a–d, respectively. Note that we ignore overlap components $q_{\alpha\beta}^{xy}$ and $q_{\alpha\beta}^{yx}$ throughout because we believe they play no role as order parameters.
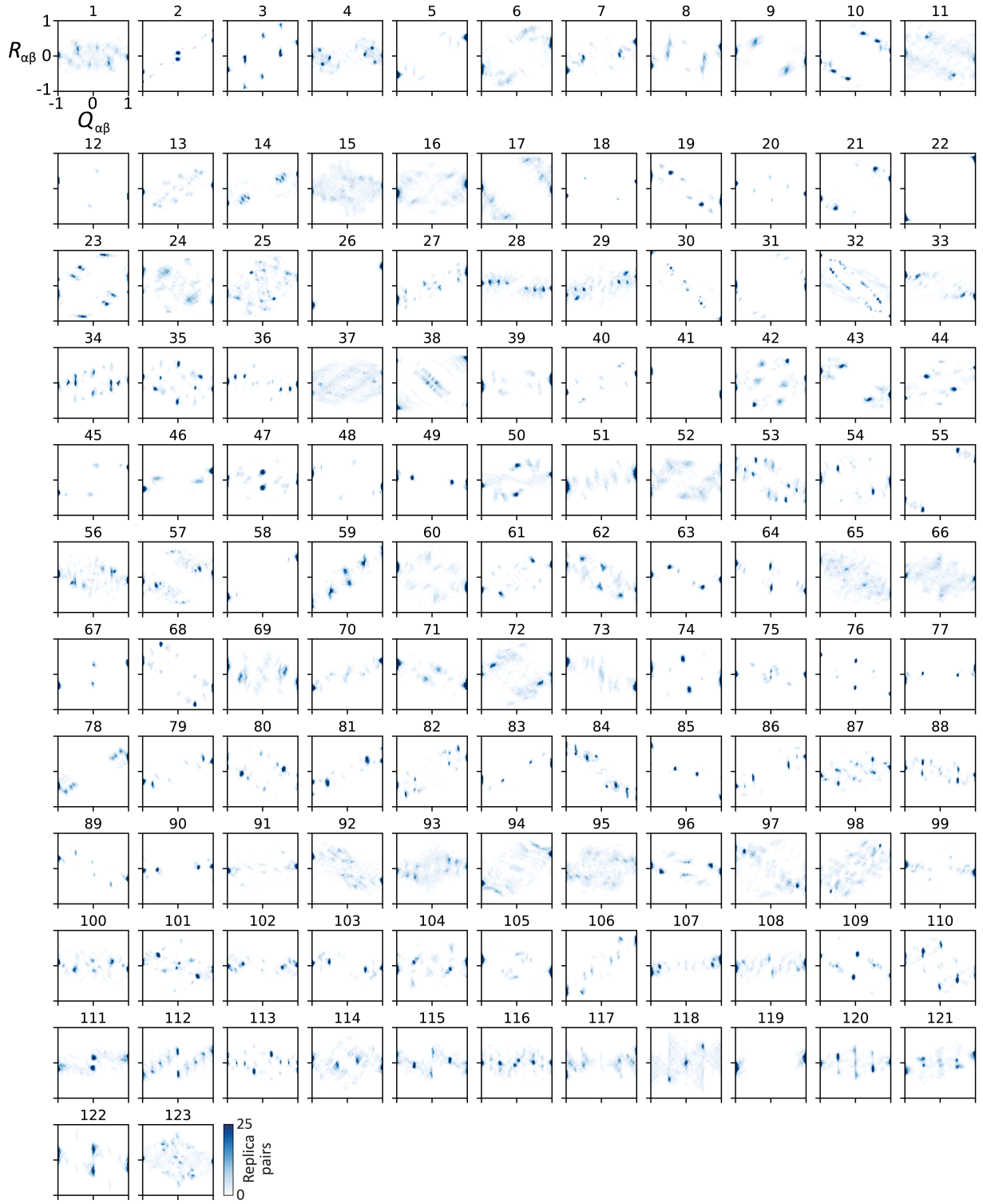
FIG. S15. All experimentally measured spin-overlap distributions.